

Orbital multiferroicity in pentalayer rhombohedral graphene

<https://doi.org/10.1038/s41586-023-06572-w>

Received: 11 April 2023

Accepted: 25 August 2023

Published online: 18 October 2023

 Check for updates

Tonghang Han^{1,6}, Zhengguang Lu^{1,6}, Giovanni Scuri^{2,3}, Jiho Sung^{2,3}, Jue Wang^{2,3}, Tianyi Han¹, Kenji Watanabe⁴, Takashi Taniguchi⁵, Liang Fu¹, Hongkun Park^{2,3} & Long Ju^{1✉}

Ferroic orders describe spontaneous polarization of spin, charge and lattice degrees of freedom in materials. Materials exhibiting multiple ferroic orders, known as multiferroics, have important parts in multifunctional electrical and magnetic device applications^{1–4}. Two-dimensional materials with honeycomb lattices offer opportunities to engineer unconventional multiferroicity, in which the ferroic orders are driven purely by the orbital degrees of freedom and not by electron spin. These include ferro-valleytricity corresponding to the electron valley⁵ and ferro-orbital-magnetism⁶ supported by quantum geometric effects. These orbital multiferroics could offer strong valley–magnetic couplings and large responses to external fields—enabling device applications such as multiple-state memory elements and electric control of the valley and magnetic states. Here we report orbital multiferroicity in pentalayer rhombohedral graphene using low-temperature magneto-transport measurements. We observed anomalous Hall signals R_{xy} with an exceptionally large Hall angle ($\tan\theta_H > 0.6$) and orbital magnetic hysteresis at hole doping. There are four such states with different valley polarizations and orbital magnetizations, forming a valley–magnetic quartet. By sweeping the gate electric field E , we observed a butterfly-shaped hysteresis of R_{xy} connecting the quartet. This hysteresis indicates a ferro-valleytronic order that couples to the composite field $\mathbf{E} \cdot \mathbf{B}$ (where B is the magnetic field), but not to the individual fields. Tuning E would switch each ferroic order independently and achieve non-volatile switching of them together. Our observations demonstrate a previously unknown type of multiferroics and point to electrically tunable ultralow-power valleytronic and magnetic devices.

Two-dimensional (2D) materials with honeycomb lattices feature electron valley as an internal degree of freedom that resembles spin. But owing to its orbital nature, the valley is easier to control through an electric field, magnetic field and circular polarization of light^{7–9}. The possibility of using valley for information storage, transportation and processing has enabled intensive research in the field known as valleytronics⁵. In parallel, these materials host quantum geometric effects^{6–10} that can be controlled by tuning the band structure, including the valley-dependent Hall effect and orbital magnetism^{6–10}. The latter could exhibit a much larger coupling to the magnetic field compared with electron spin^{10,11}. These orbital-degrees-driven phenomena provide a fertile ground for previously unknown ferroic orders, which warrants large responses to external fields and multifunctional device applications. For example, information could be stored in several states with different combinations of valley and magnetic characters instead of being limited to the binary states of spin. Furthermore, these states can be manipulated conveniently by an electric field. Although orbital multiferroics provide many applications and theory proposals for realizing multiferroics in heterostructures of graphene and transition metal

dichalcogenides^{12–14}, independent switching of valley and magnetism has remained elusive.

Recently, spontaneous valley polarization and orbital magnetism induced by electron-correlation effects have been observed in rhombohedral bilayer and trilayer graphene^{15–19}, as well as in twisted graphene layers^{20–24}. Despite the observed magnetic hysteresis, the valley and orbital magnetization are always locked. This is because a large-gate electric field E is required to generate flat bands for Stoner instability^{15–17}, or the fixed band structure in a moiré superlattice^{19–24}. The one-to-one correspondence between valley and magnetization prevents their independent control and realizing multiferroicity. In the twisted mono-bilayer graphene, flipping of orbital magnetization by charge doping in a fixed valley was observed²². The explanation relies on large edge-state-current contribution²⁵, while the magnetic moments in the bulk states are locked to the valley. In a general material setting without moiré, it is crucial to understand the contributions of bulk states to ferro-valleytronic and ferro-orbital-magnetic orders without the complications of edge states. However, orbital multiferroicity in natural crystals has not been observed.

¹Department of Physics, Massachusetts Institute of Technology, Cambridge, MA, USA. ²Department of Chemistry and Chemical Biology, Harvard University, Cambridge, MA, USA. ³Department of Physics, Harvard University, Cambridge, MA, USA. ⁴Research Center for Electronic and Optical Materials, National Institute for Materials Science, Tsukuba, Japan. ⁵Research Center for Materials Nanoarchitectonics, National Institute for Materials Science, Tsukuba, Japan. ⁶These authors contributed equally: Tonghang Han, Zhengguang Lu. ✉e-mail: longju@mit.edu

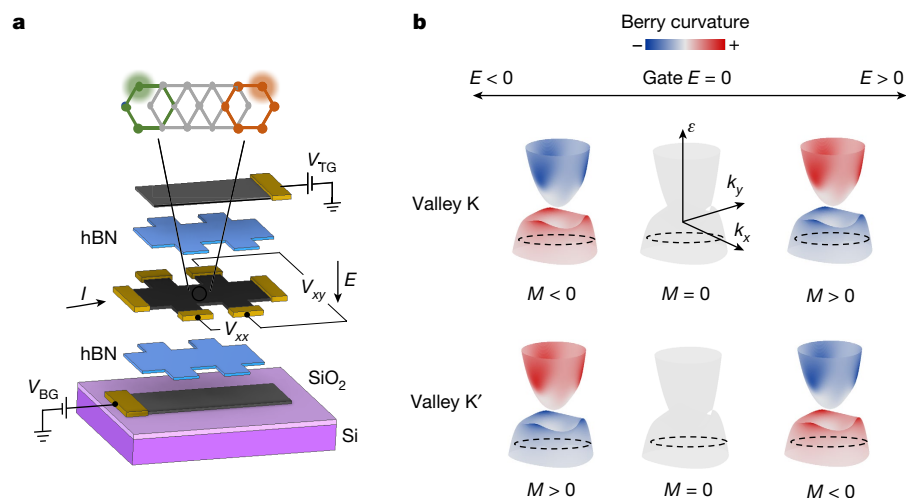


Fig. 1 | Gate-induced Berry curvature and valley-magnetic quartet in pentalayer graphene with rhombohedral stacking. **a**, Schematic of the dual-gated Hall bar device, featuring the top view of the atomic structure of pentalayer rhombohedral graphene. The highlighted orbitals located at the bottom and top layers of pentalayer graphene dominate the wavefunctions of the low-energy bands. **b**, Colour-coded band structure in the K and K' valleys,

showing the Berry curvature distribution at varied gate electric field E . The valence band is flatter than the conduction band and more susceptible to electron-correlation effects. The Berry curvature and orbital magnetic moment (M) of the hole states change signs as E changes sign. Berry curvatures in the two valleys sum up to zero, to ensure time-reversal symmetry. The four states at non-zero E form a valley-magnetic quartet.

Here we explore orbital multiferroicity in pentalayer graphene with rhombohedral stacking. We purposely twist the angle between graphene and hexagonal boron nitride (hBN) layers away from zero degrees to avoid moiré effects^{15,26}. As shown in Fig. 1a, orbitals located at the two highlighted sublattices dominate the electronic states near zero energy. Figure 1b shows the band structure and Berry curvature distribution in pentalayer graphene based on a tight-binding calculation²⁷. At $E = 0 \text{ V nm}^{-1}$, the two bands feature great flatness and a substantially larger density of states than those in thinner graphene (Extended Data Fig. 3). At the same time, the inversion symmetry of the system ensures a zero Berry curvature. When the bandgap is opened by E , states near the band edges acquire a non-zero Berry curvature^{10,27–29}. The signs of the Berry curvature, the anomalous Hall resistance R_{xy} and the orbital magnetization depend on the valley index and the sign of E . These results clearly show that valley and orbital magnetism are two separate order parameters in rhombohedral graphene. It is therefore possible to have a quartet of valley-polarized states, (K, +M), (K, -M), (K', +M) and (K', -M), each with the Fermi-surface cuts through one of the four bands. The flat bands with tunable Berry curvature in pentalayer graphene provide a fertile ground for electron-correlation and quantum-geometry effects. The spin character of bands is not shown as it is irrelevant to the observations and discussions.

Spontaneous ferro-orbital-magnetism

Figure 2a shows R_{xx} as a function of the electron density n_e and E in zero magnetic field. With hole doping in the flat band, a bubble-shaped region ('bubble' for simplicity) that is symmetric about $E = 0$ emerges. With an out-of-plane magnetic field $B = 1.8 \text{ T}$, quantum oscillation features appear within the bubble as shown in Fig. 2b. The period of oscillation corresponds to two isospin flavours at the Fermi level (Extended Data Fig. 2), indicating an isospin-symmetry-broken half-metal state. This bubble is absent in the previous reports of rhombohedral graphene^{15–19,30,31}.

Figure 2c shows the R_{xy} at $B = 0.5 \text{ T}$. Outside the bubble, a small R_{xy} signal prevails and corresponds to the normal Hall signal. Within the bubble, large anomalous Hall signals appear in a wings-shaped region

('wings' for simplicity). The wings largely overlap with the region that shows quantum oscillations in Fig. 2b. Figure 2d shows R_{xy} at different E s at $n_e = -0.55 \times 10^{12} \text{ cm}^{-2}$, as B is scanned back and forth. No hysteresis is seen at $E = 10 \text{ mV nm}^{-1}$, whereas clear hysteresis can be seen within the wings. The coercive field ΔB_c decreases, whereas the jump in Hall resistance ΔR_{xy} increases, as E is increased in amplitude. The values of ΔB_c and ΔR_{xy} as a function of E are summarized in Fig. 2e. We note that the anomalous Hall angle is exceptionally large, with the largest $\tan\theta_H > 0.6$ (refs. 32,33).

Combining the isospin-symmetry breaking with the anomalous Hall signal, we conclude that the wings region is valley-polarized. The magnetic hysteresis loop demonstrates a ferro-orbital-magnetism, in which spin is not involved. Figure 2d shows the states at large B values. The Fermi surface is highlighted as a dashed circle, which cuts through the valence band in only one valley. Qualitatively, sweeping B switches both the valley and magnetization at the same time. By switching the sign of E at fixed B , the valley order is flipped whereas the magnetization remains because the magnetic field always chooses the valley that minimizes the magnetic energy. Microscopically, the close-to-linear relation between ΔR_{xy} and $|E|$ is because of the field-controlled Berry curvature distribution and can be reproduced by our tight-binding calculation (Extended Data Fig. 4). This demonstrates a mechanism to achieve electrical tuning of orbital magnetism, whereas its counterpart for spin magnetism has been demonstrated³⁴. We note the value of ΔB_c and ΔR_{xy} change in opposite ways when E is changed, as the product $\mathbf{M} \cdot \mathbf{B}$ (where M is the average orbital magnetic moment) needs to overcome an energy barrier to have the magnetization flipped. The value of M is hard to measure directly through transport measurements because of the small size of our device, but the value can be extracted indirectly as shown later.

The valley-polarized half-metal state in pentalayer graphene is induced by the electron-correlation effect in the flat band, in the form of a valley-exchange interaction^{35–37}. Although other isospin-symmetry-broken states have been observed in Bernal bilayer graphene and ABC trilayer graphene (only at large E)^{15–17}, there was no sign of valley-polarized half-metal states. Moreover, this state resides at around zero E , which leads to an important consequence as shown next.

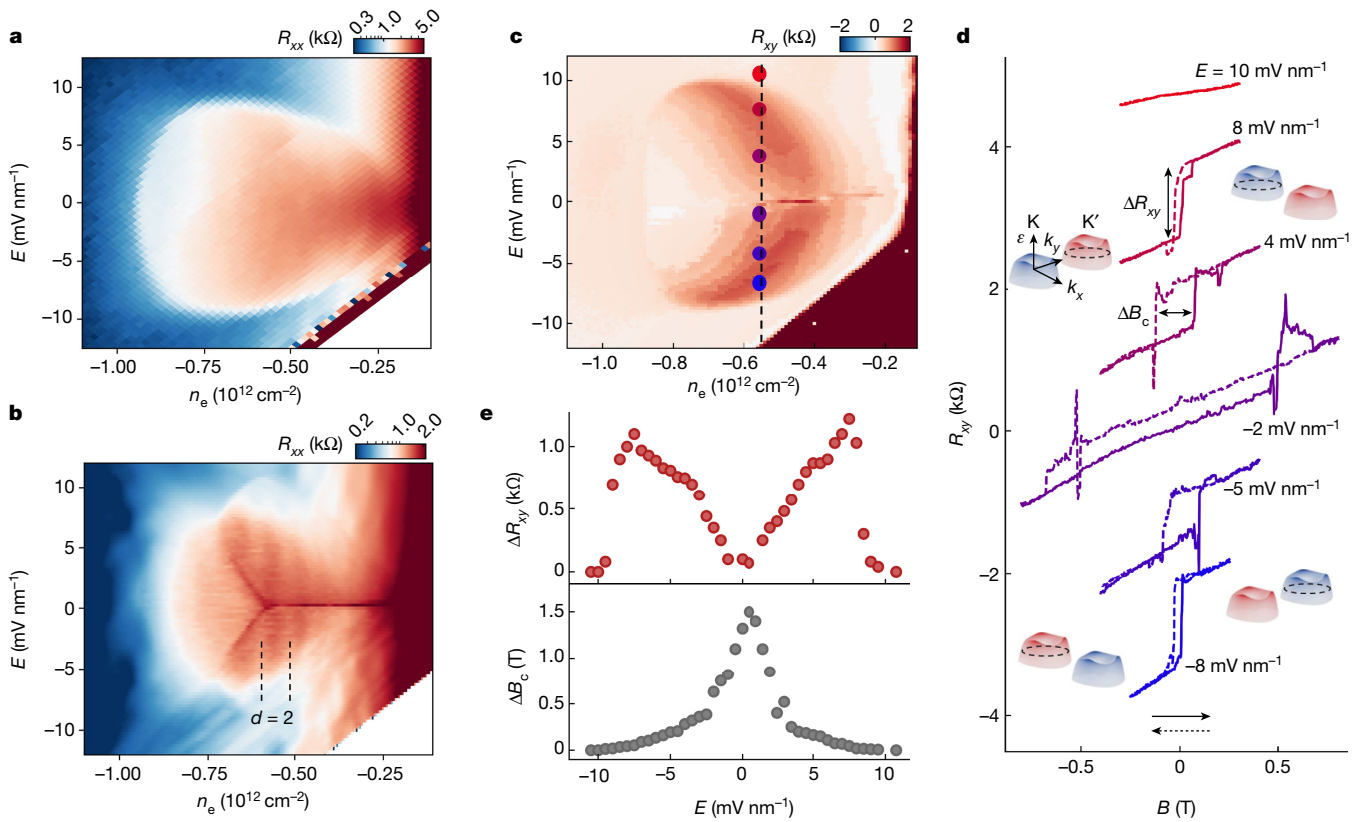


Fig. 2 | Ferro-orbital-magnetism in a valley-polarized half-metal.

a, b, Two-dimensional colour maps of the longitudinal resistance R_{xx} at 0 T (**a**) and 1.8 T (**b**) out-of-plane magnetic fields. A bubble-shaped region appears when the flat valence band is doped by holes. At 1.8 T, quantum oscillations appear in part of the bubble and the period in density of states corresponds to two isospin flavours (degeneracy $d = 2$) at the Fermi level. **c**, Two-dimensional colour map of the Hall resistance R_{xy} at $B = 0.5$ T in the same range as in **a** and **b**. An anomalous Hall signal appears in a wings-shaped region that largely overlaps with where quantum oscillations are seen in **b**, indicating orbital magnetism due to valley polarization in this half-metal region. **d**, R_{xy} as the magnetic field B is scanned, showing clear hysteresis loops within the wings.

Ferro-valleytricity

We further explore the valley and orbital magnetic orders by scanning the electric field E at $B = 20$ mT, as shown in Fig. 3a, b. Surprisingly, the sign of R_{xy} switches as the scanning direction switches if we focus on the wings. Figure 3c shows a line-cut at $n_e = -0.55 \times 10^{12} \text{ cm}^{-2}$, which shows a butterfly-shaped hysteresis loop ('butterfly' for simplicity) within the wings. Repeating the measurements in Fig. 3c at -20 mT, a butterfly with an opposite winding direction appears as shown in Fig. 3e. We note that the small magnetic field is used to suppress the fluctuations of the whole magnetization (Extended Data Fig. 8).

On the basis of earlier discussions, we show the band structure and Fermi level corresponding to different states in Fig. 3c. When E is scanned into the wings, the system selects the valley that minimizes the magnetic energy $-\mathbf{M} \cdot \mathbf{B}$. Scanning through zero E , the valley polarization persists at the cost of a higher magnetic energy (because R_{xy} and orbital magnetization are flipped). Figure 3d shows the valley polarization V (defined as +1 for K valley and -1 for K' valley) extracted from Fig. 3c. It features a hysteresis loop and a ferroic order called ferro-valleytricity—the spontaneous polarization and switching of the valley order. Even at zero E , the valley polarization exists although the orbital magnetization is zero, in contrast to a non-zero

Curves correspond to dots with the same colour in **c** at $n_e = -0.55 \times 10^{12} \text{ cm}^{-2}$ and different E s, and are shifted vertically for clarity. Solid and dashed curves correspond to forwards and backwards scanning of the B field, respectively. Schematics of the valence band alignment and Fermi surface are shown for representative states. The bands are colour-coded by the value of Berry curvature, the same as in Fig. 1b. **e**, The anomalous Hall signal ΔR_{xy} and the coercive field ΔB_c extracted from **d** along the dashed line in **c**. ΔR_{xy} is the amplitude of the abrupt jump of the transverse resistance that is extracted by averaging the changes of R_{xy} at the two vertical edges of the magnetic hysteresis loop. ΔR_{xy} increases, whereas ΔB_c decreases with increasing amplitude of E .

magnetization at valley-polarized states in other graphenes systems^{15,19–23}. These observations show that the valley polarization and orbital magnetization are two different order parameters of the ground state, distinct from those in the quarter-metal of trilayer graphene. Moreover, the butterfly hysteresis can exist in pentalayer graphene because the valley-polarized half-metal resides at around zero E . But in rhombohedral trilayer graphene¹⁵, the valley polarization is lost when E is scanned to outside the quarter-metal state, and a butterfly was not observed.

We note that the conjugate field of the valley polarization is $\mathbf{E} \cdot \mathbf{B}$. This can be seen from the winding directions of the valley polarization in Fig. 3d, e: the two hysteresis loops under positive and negative B wind in opposite ways, but they can be unified if we plot R_{xy} versus $\mathbf{E} \cdot \mathbf{B}$ instead of E (Extended Data Fig. 6). This is consistent with the relation between orbital magnetization and valley shown in Fig. 1b.

We provide a simple picture to understand both the ferro-orbital-magnetism and ferro-valleytricity observed in our device. The coupling between orbital magnetization and valley order can be described by a free energy $F = -\alpha V \mathbf{E} \cdot \mathbf{B}$ per hole, where α is a constant independent of E , V and B . In the case of scanning B , F can be viewed as $-(\alpha V \mathbf{E}) \cdot \mathbf{B}$, where $\alpha V \mathbf{E}$ is effectively the average orbital magnetic moment and B is the corresponding conjugate field. The average orbital magnetic moment $\alpha V \mathbf{E} = g \mu_B$ (where μ_B is the Bohr magneton and

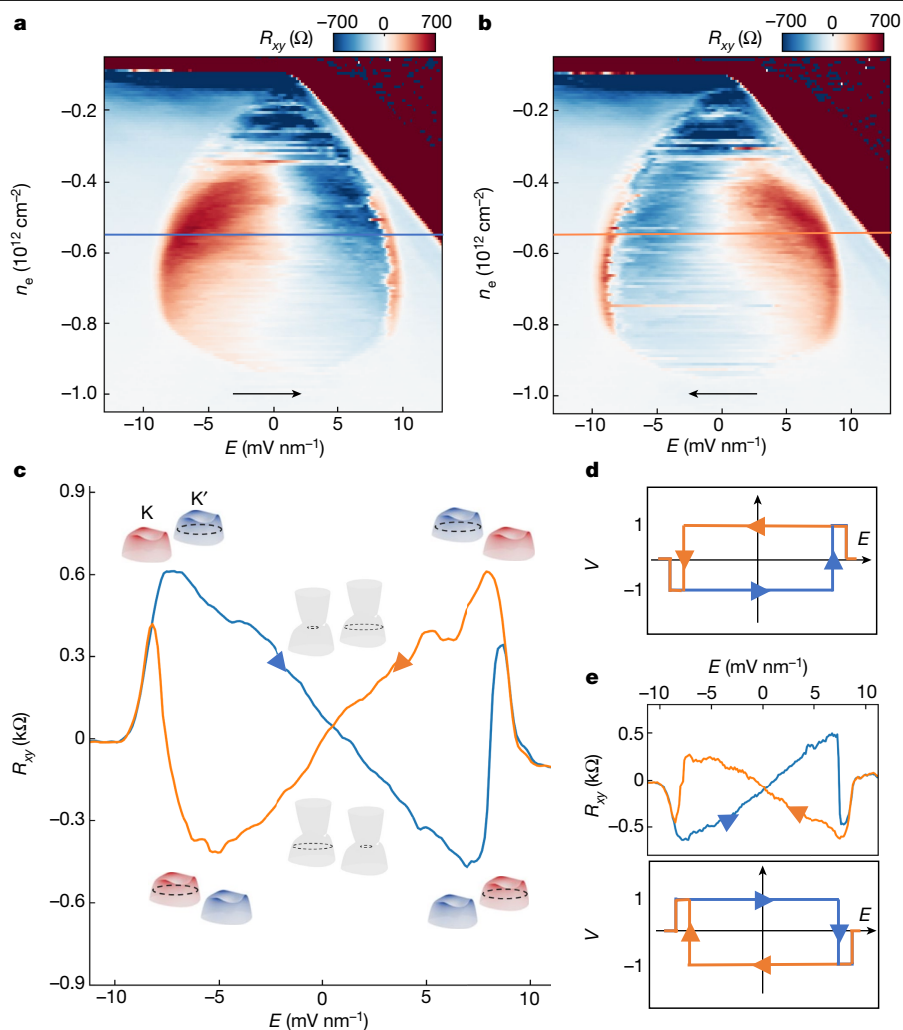


Fig. 3 | Ferro-valleytricity. **a, b**, Two-dimensional colour maps of R_{xy} corresponding to forwards (**a**) and backwards (**b**) scanning of E , at a small magnetic field $B = 20$ mT. **c**, R_{xy} at $n_e = -0.55 \times 10^{12} \text{ cm}^{-2}$, corresponding to the lines shown in **a** and **b**. Hysteresis behaviour is seen as a butterfly shape. This indicates that the valley polarization persists as E and changes signs until close to the boundary and out of the wings. Schematics of the valence band alignment and Fermi surface are shown for representative states. The bands are colour-coded by the value of Berry curvature, same as in Fig. 1b. The sharp

spikes right before exiting the butterfly are because of the flipping of valley and R_{xy} induced by the magnetic coupling $-\mathbf{M} \cdot \mathbf{B}$. **d**, Plot of valley polarization V corresponds to the R_{xy} plot in **a**, featuring a hysteresis loop and a ferro-valleytronic order. **e**, The same plots as in **c** and **d** for a small negative magnetic field $B = -20$ mT. The directions of winding in V are opposite to those in **d**, but they can be unified when plotting versus the conjugate field $\mathbf{E} \cdot \mathbf{B}$ (Extended Data Fig. 6).

g is the g -factor) will be extracted from a toy model in the next section. In the case of scanning E , F can be viewed as $-(\alpha V)(\mathbf{E} \cdot \mathbf{B})$, where αV is effectively the valley moment and $\mathbf{E} \cdot \mathbf{B}$ is the corresponding conjugate field.

B- and T-dependent ferro-valleytricity

Having established ferro-valleytricity, we further explore its response to B and elevated temperature T . Figure 4a,b shows the evolution of butterfly at increased B , taken at $T = 300$ mK and $n_e = -0.55 \times 10^{12} \text{ cm}^{-2}$ (see Extended Data Fig. 7 for other densities). At small B , the butterfly remains similar to that in Fig. 3c. As $|B|$ is increased, the range of E showing hysteresis gradually shrinks and eventually disappears at about 0.6 T. Figure 4c shows line-cuts corresponding to the solid and dashed lines in Fig. 4a,b, where the butterfly gradually shrinks and evolves into an ‘M’ or ‘W’ shape. We define the critical electric field at which the butterfly terminates as E_B . At $B = -20$ mT, Fig. 4d shows R_{xy} as E is scanned at elevated T . Similar to its response to B , the butterfly

gradually evolves into a ‘W’ shape as the temperature is increased to around 2 K. We define the critical electric field at which the butterfly terminates as E_T . Figure 4e summarizes E_B and E_T as a function of B and T , respectively.

A model to qualitatively describe the response to B and T is shown in Fig. 4f. The free energy of Ising-coupled orbital magnets has two local minima at $-M$ and $+M$ respectively, where $\pm M$ is the average orbital magnetic moment per hole. An energy barrier Δ prevents the flipping of the magnetization between $-M$ and $+M$. At E_B and E_T , this barrier is overcome by a combination of the thermal energy $k_B T$ (where k_B is the Boltzmann constant) and the magnetic energy $\mathbf{M} \cdot \mathbf{B}$. As a result, the device switches from the local minimal energy state (K, $-M$) to the global minimal energy state (K', $+M$), and the butterfly is terminated. Further analysis of data in Fig. 4e enables the extraction of the g -factor as shown in Fig. 4g (Methods), which agrees with previous literature^{10,28}. This average orbital magnetic moment per hole is about 10 times bigger than that of electron spin, which enables much stronger coupling with a magnetic field.

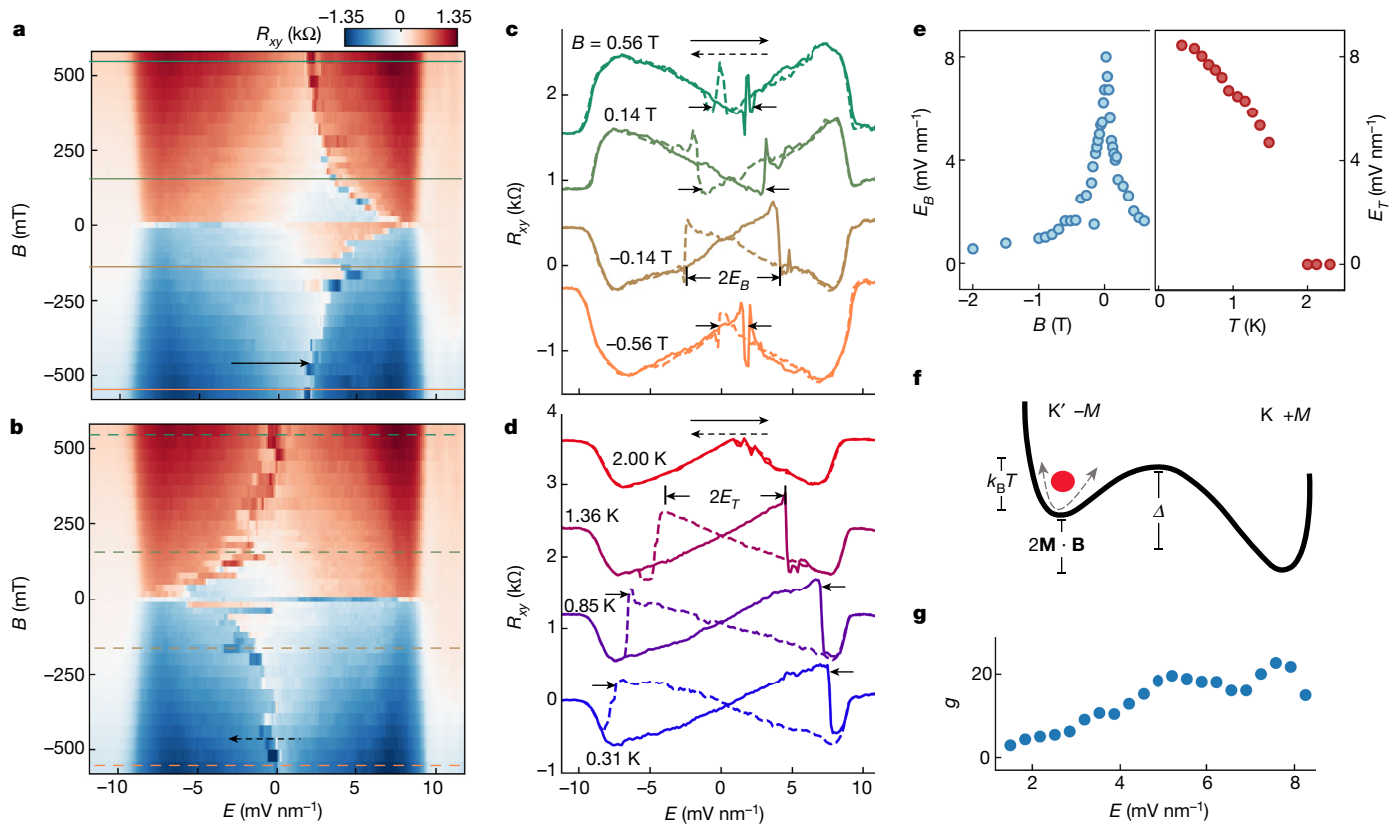


Fig. 4 | Ferro-valleytricity controlled by magnetic field and temperature. **a, b**, Two-dimensional colour maps of R_{xy} , corresponding to forwards **(a)** and backwards **(b)** scanning of E at different magnetic fields, at $n_e = -0.55 \times 10^{12} \text{ cm}^{-2}$. When B is small, ferro-valleytricity dominates the device behaviour. At above approximately 0.6 T, the R_{xy} and V are completely determined by the magnetic field while the butterfly disappears. **c**, Line-cuts corresponding to the solid lines in **a** and the dashed lines in **b**, showing that the butterfly gradually shrinks in E and eventually evolves into an ‘M’ or ‘W’ shape. E_B indicated by the arrows is the critical field at which the butterfly is terminated. **d**, R_{xy} as E is scanned at

different temperatures at $n_e = -0.55 \times 10^{12} \text{ cm}^{-2}$ and $B = -20 \text{ mT}$. The butterfly and ferro-valleytricity gradually disappear as the temperature is increased, similar to the behaviours when B is increased. E_T is the critical field at which the butterfly is terminated. **e**, Critical fields E_B and E_T from **c** and **d**, respectively. **f**, Schematic to explain the flipping of R_{xy} at the critical fields E_B and E_T . The flipping happens when the magnetic energy $\mathbf{M} \cdot \mathbf{B}$ and thermal energy $k_B T$ add up to overcome the energy barrier Δ . **g**, Effective g -factor of the average orbital magnetic moment as a function of E extracted from **e**.

Orbital multiferroicity and switching

The ferro-valleytronic order enriches the family of ferroic orders in solids. Figure 5a compares ferro-valleytricity with conventional ferroic orders and conjugate fields. The valley order breaks both the inversion symmetry and the time-reversal symmetry, similar to that of ferro-toroidicity³⁸. This can be seen from the (different form of) product of E and B as conjugate fields in both cases. The coexistence of ferro-valleytricity and the orbital ferro-magnetism represent a previously unknown type of multiferroics in which both orders ultimately originate from the orbital degree of electrons but not spin. These two orders couple strongly with each other, similar to that in type-II multiferroics². First, at fixed B , the conjugate field of the valley order ($\mathbf{E} \cdot \mathbf{B}$) can continuously tune the orbital magnetic moment as shown in Figs. 3c and 4g, similar to the magneto-electric coupling in conventional type-II multiferroics. Second, the emergence of ferro-valleytricity and ferro-orbital-magnetism happen at a similar temperature of $T = 2 \text{ K}$ (Fig. 4d and Extended Data Fig. 5). These coincident critical temperatures are typical of type-II multiferroics, in which one order spontaneously polarizes the other order through their coupling.

The gate electric field plays an important part in both ferroic orders as it contributes to the conjugate field of the valley order and controls the orbital magnetization. We can therefore use E to control the valley and orbital magnetization independently as shown in Fig. 5b.

The valley-magnetic quartet states are connected by the butterfly in Fig. 3a, including $(K, +M)$, $(K, -M)$, $(K', +M)$ and $(K', -M)$. At small B , we can choose different routes along the butterfly to switch the valley repeatedly and keep the magnetization as shown in the blue-shaded part of Fig. 5b, or to keep the valley and switch the magnetization repeatedly as shown in the yellow-shaded part of Fig. 5b. Furthermore, the two ferro-magnetic states at the same E —for example, $(K, +M)$ and $(K', -M)$ can be switched non-volatily as shown in Fig. 5c.

The switching between the valley-magnetic quartet states requires only a change of the gate electric field, but not current flowing through graphene. This is preferable to the current-induced switching of the magnetization from the power consumption point of view, which was the case in twisted bilayer graphene as well as conventional magnetic switches^{20,21,39,40}.

Conclusion

We demonstrated orbital multiferroicity in the flat bands of crystal-line pentalayer graphene, which features co-existed but independent ferro-valleytricity and orbital-ferro-magnetism. It enriches the family of electronic phases of matter driven by the co-existing electron-correlation and quantum-geometry effects. Our experiment opens up possibilities in harnessing the electron valley and orbital magnetism for multifunctional device applications in valleytronics and magnetics.

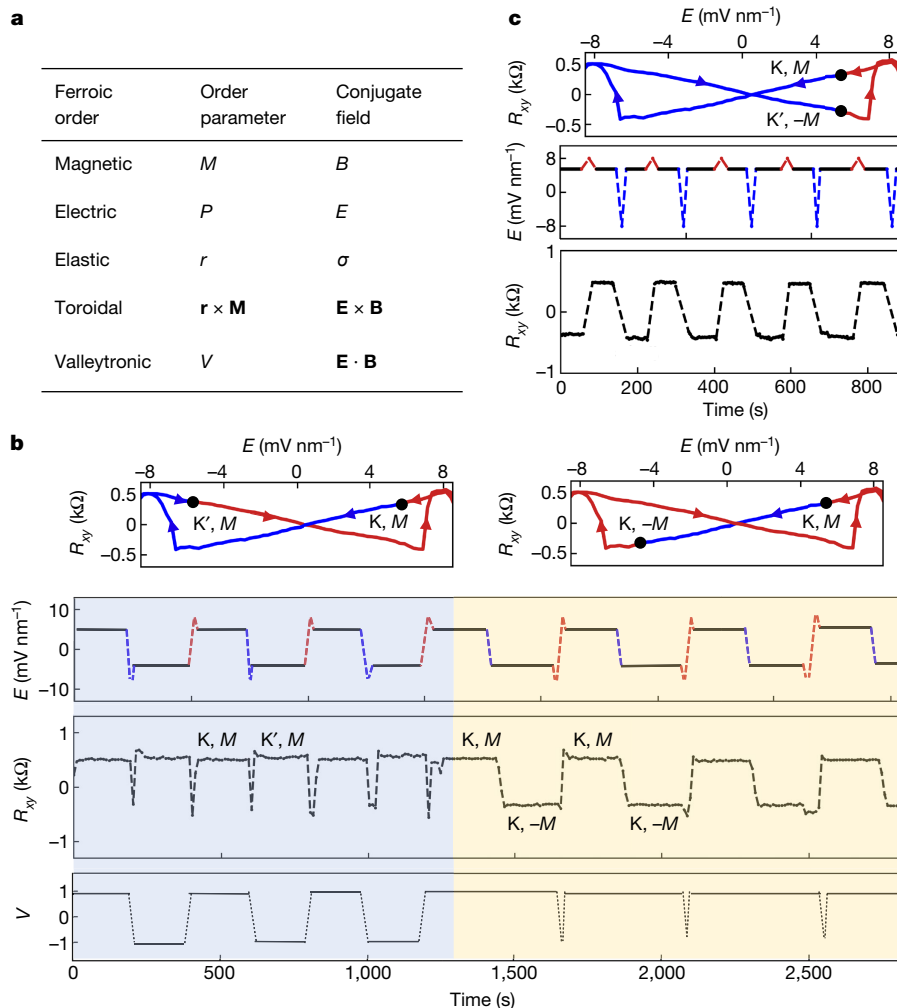


Fig. 5 | Electrical control of the orbital multiferroic. **a**, Ferroic orders and the corresponding conjugate fields. The ferro-valleytronic order breaks both inversion (due to the E field) and time-reversal symmetry (due to the B field), similar to the ferro-toroidal order. The ferro-valleytronic order and ferro-orbital-magnetic order form an orbital multiferroic. **b**, Switching of the valley polarization V (blue) and orbital magnetic moment M (yellow) independently

by sweeping the gate electric field E . Top, the path of switching along the butterfly between the two static states labelled by the two dots. The colour of the paths matches that of the switching pulse and the arrows label the scanning direction. A small magnetic field $B = 20$ mT is applied here. **c**, Non-volatile switching of M and V together using a gate electric field.

Online content

Any methods, additional references, Nature Portfolio reporting summaries, source data, extended data, supplementary information, acknowledgements, peer review information; details of author contributions and competing interests; and statements of data and code availability are available at <https://doi.org/10.1038/s41586-023-06572-w>.

- Eerenstein, W., Mathur, N. D. & Scott, J. F. Multiferroic and magnetoelectric materials. *Nature* **442**, 759–765 (2006).
- Fiebig, M., Lottermoser, T., Meier, D. & Trassin, M. The evolution of multiferroics. *Nat. Rev. Mater.* **1**, 16046 (2016).
- Spaldin, N. A., Cheong, S. W. & Ramesh, R. Multiferroics: past, present, and future. *Phys. Today* **63**, 38–43 (2010).
- Jin, W. et al. Observation of a ferro-rotational order coupled with second-order nonlinear optical fields. *Nat. Phys.* **16**, 42–46 (2019).
- Xu, X., Yao, W., Xiao, D. & Heinz, T. F. Spin and pseudospins in layered transition metal dichalcogenides. *Nat. Phys.* **10**, 343–350 (2014).
- Xiao, D., Chang, M.-C. & Niu, Q. Berry phase effects on electronic properties. *Rev. Mod. Phys.* **82**, 1959–2007 (2010).
- Mak, K. F., McGill, K. L., Park, J. & McEuen, P. L. The valley Hall effect in MoS₂ transistors. *Science* **344**, 1489–1492 (2014).
- Ju, L. et al. Topological valley transport at bilayer graphene domain walls. *Nature* **520**, 650–655 (2015).

- Yin, J. et al. Tunable and giant valley-selective Hall effect in gapped bilayer graphene. *Science* **375**, 1398–1402 (2022).
- Xiao, D., Yao, W. & Niu, Q. Valley-contrasting physics in graphene: magnetic moment and topological transport. *Phys. Rev. Lett.* **99**, 236809 (2007).
- Ju, L. et al. Tunable excitons in bilayer graphene. *Science* **358**, 907–910 (2017).
- Tong, W.-Y., Gong, S.-J., Wan, X. & Duan, C.-G. Concepts of ferrovalley material and anomalous valley Hall effect. *Nat. Commun.* **7**, 13612 (2016).
- Abouelkomsan, A., Bergholtz, E. J. & Chatterjee, S. Multiferroicity and topology in twisted transition metal dichalcogenides. Preprint at <https://arxiv.org/abs/2210.14918> (2022).
- Wang, T., Vila, M., Zaletel, M. P. & Chatterjee, S. Electrical control of spin and valley in spin-orbit coupled graphene multilayers. Preprint at <https://arxiv.org/abs/2303.04855> (2023).
- Zhou, H. et al. Half- and quarter-metals in rhombohedral trilayer graphene. *Nature* **598**, 429–433 (2021).
- Zhou, H. et al. Isospin magnetism and spin-polarized superconductivity in Bernal bilayer graphene. *Science* **375**, 774–778 (2022).
- de la Barrera, S. C. et al. Cascade of isospin phase transitions in Bernal-stacked bilayer graphene at zero magnetic field. *Nat. Phys.* **18**, 771–775 (2022).
- Shi, Y. et al. Electronic phase separation in multilayer rhombohedral graphite. *Nature* **584**, 210–214 (2020).
- Chen, G. et al. Tunable correlated Chern insulator and ferromagnetism in a moiré superlattice. *Nature* **579**, 56–61 (2020).
- Sharpe, A. L. et al. Emergent ferromagnetism near three-quarters filling in twisted bilayer graphene. *Science* **365**, 605–608 (2019).
- Serlin, M. et al. Intrinsic quantized anomalous Hall effect in a moiré heterostructure. *Science* **367**, 900–903 (2020).
- Polshyn, H. et al. Electrical switching of magnetic order in an orbital Chern insulator. *Nature* **588**, 66–70 (2020).

23. Chen, S. et al. Electrically tunable correlated and topological states in twisted monolayer-bilayer graphene. *Nat. Phys.* **17**, 374–380 (2020).
24. Li, T. et al. Quantum anomalous Hall effect from intertwined moiré bands. *Nature* **600**, 641–646 (2021).
25. Zhu, J., Su, J. J. & MacDonald, A. H. Voltage-controlled magnetic reversal in orbital Chern insulators. *Phys. Rev. Lett.* **125**, 227702 (2020).
26. Yang, J. et al. Spectroscopy signatures of electron correlations in a trilayer graphene/hBN moiré superlattice. *Science* **375**, 1295–1299 (2022).
27. Min, H. & MacDonald, A. H. Electronic structure of multilayer graphene. *Prog. Theor. Phys. Suppl.* **176**, 227–252 (2008).
28. Zhang, F., Jung, J., Fiete, G. A., Niu, Q. & MacDonald, A. H. Spontaneous quantum Hall states in chirally stacked few-layer graphene systems. *Phys. Rev. Lett.* **106**, 156801 (2011).
29. Koshino, M. & McCann, E. Trigonal warping and Berry's phase $N\pi$ in ABC-stacked multilayer graphene. *Phys. Rev. B* **80**, 165409 (2009).
30. Weitz, R. T., Allen, M. T., Feldman, B. E., Martin, J. & Yacoby, A. Broken-symmetry states in doubly gated suspended bilayer graphene. *Science* **330**, 812–816 (2010).
31. Velasco, J. Jr et al. Transport spectroscopy of symmetry-broken insulating states in bilayer graphene. *Nat. Nanotechnol.* **7**, 156–160 (2012).
32. Nagaosa, N., Sinova, J., Onoda, S., MacDonald, A. H. & Ong, N. P. Anomalous Hall effect. *Rev. Mod. Phys.* **82**, 1539–1592 (2010).
33. Liu, E. et al. Giant anomalous Hall effect in a ferromagnetic kagome-lattice semimetal. *Nat. Phys.* **14**, 1125–1131 (2018).
34. Matsukura, F., Tokura, Y. & Ohno, H. Control of magnetism by electric fields. *Nat. Nanotechnol.* **10**, 209–220 (2015).
35. Dong, Z., Davydova, M., Ogunnaike, O. & Levitov, L. Isospin- and momentum-polarized orders in bilayer graphene. *Phys. Rev. B* **107**, 075108 (2021).
36. Szabó, A. L. & Roy, B. Competing orders and cascade of degeneracy lifting in doped Bernal bilayer graphene. *Phys. Rev. B* **105**, L201107 (2022).
37. Huang, C. et al. Spin and orbital metallic magnetism in rhombohedral trilayer graphene. *Phys. Rev. B* **107**, L121405 (2023).
38. Gnewuch, S. & Rodríguez, E. E. The fourth ferroic order: current status on ferrotoroidic materials. *J. Solid State Chem.* **271**, 175–190 (2019).
39. Fan, Y. et al. Magnetization switching through giant spin-orbit torque in a magnetically doped topological insulator heterostructure. *Nat. Mater.* **13**, 699–704 (2014).
40. He, W.-Y., Goldhaber-Gordon, D. & Law, K. T. Giant orbital magnetoelectric effect and current-induced magnetization switching in twisted bilayer graphene. *Nat. Commun.* **11**, 1650 (2020).

Publisher's note Springer Nature remains neutral with regard to jurisdictional claims in published maps and institutional affiliations.

Springer Nature or its licensor (e.g. a society or other partner) holds exclusive rights to this article under a publishing agreement with the author(s) or other rightsholder(s); author self-archiving of the accepted manuscript version of this article is solely governed by the terms of such publishing agreement and applicable law.

© The Author(s), under exclusive licence to Springer Nature Limited 2023

Device fabrication

The pentalayer graphene and hBN flakes were prepared by mechanical exfoliation onto SiO₂/Si substrates. The rhombohedral domains of pentalayer graphene were identified using near-field infrared microscopy⁸, confirmed with Raman spectroscopy and isolated by cutting with a Bruker atomic force microscope⁴¹. The van der Waals heterostructure was made following a dry transfer procedure. We picked up the top hBN and pentalayer graphene using polypropylene carbonate film and landed it on a prepared bottom stack consisting of an hBN and graphite bottom gate. We intentionally misaligned the straight edges of the flakes to avoid the formation of the moiré superlattice. The device was then etched into a Hall bar structure using standard e-beam lithography and reactive-ion etching. We deposited Cr/Au contact electrodes and an NiCr alloy top layer to form a dual-gate device.

Transport measurement

The device was measured in a Bluefors LD250 dilution refrigerator with an electronic temperature of around 100 mK. Part of the data was taken in the National High Magnetic Field Laboratory, Tallahassee. Stanford Research Systems SR830 lock-in amplifiers were used to measure the longitudinal and Hall resistance R_{xx} and R_{xy} with an a.c. voltage bias of 200 μ V at a frequency of 17.77 Hz. Keithley 2400 sourcemeters were used to apply the top- and bottom-gate voltages. Top-gate voltage (V_t) and bottom-gate voltage (V_b) were swept to adjust the doping density $n_e = (C_t V_t + C_b V_b)/e$ and electric field $E = (V_t/d_t - V_b/d_b)/2$, where C_t and C_b are top- and bottom-gate capacitance per area calculated from the Landau fan diagram.

Phase diagram of pentalayer rhombohedral graphene

Extended Data Fig. 1c,d shows the colour plots of four-probe resistance R_{xx} as a function of carrier density n and displacement field E for the hole doping side and electron doping side measured at $B = 0$ at a temperature of 100 mK. Coloured dots label different phases, including band insulator, correlated insulator, spin-polarized half-metal (SPHM), isospin-polarized quarter-metal (IPQM), unpolarized metal and valley-polarized half-metal (VPHM). The large D side of the phase diagram looks similar to that of the previous studies in bilayer and trilayer graphene^{15,16}. At the intermediate and small D side, the semi-metal and correlated insulator states emerge and dominate the neighbouring regions. The VPHM state with a waterdrop shape (labelled by a red star) is the focus of this paper.

The degeneracy of the isospin-polarized metal is inferred from the spacing of the Landau levels¹⁵. Extended Data Fig. 2a,b shows the R_{xx} as a function of n and E measured at $B = 2$ T in the VPHM state and the large-density unpolarized metal state. The Landau-level spacings indicate that the Fermi surface has two-fold in the VPHM state and four-fold degeneracy in the unpolarized metal state. The details of IPQM and SPHM states can be found in ref. 42.

Tight-binding calculation of band structure and Hall conductivity

The single-particle band structure of the rhombohedral stacked pentalayer graphene is calculated from the 10-band continuum model. The Hamiltonian and the parameters are taken from previous literature⁴³. The band structures and density of states (DOS) calculated for different layer numbers N ($2N$ -band model) are shown in Extended Data Fig. 3. The remote hopping processes lead to the trigonal warping of the band structure, resulting in deviation from $E \approx k^2$ at low energy. We note that among all layer numbers, the rhombohedral pentalayer graphene has the flattest band and the largest DOS around zero energy. This could account for the observation of correlated phases absent in Bernal bilayer and rhombohedral trilayer graphene.

Extended Data Fig. 4a shows the tight-binding calculation of band structure for rhombohedral pentalayer graphene near the K point with an interlayer potential $2\Delta = 0$ meV (black) and 16 meV (grey). Extended Data Fig. 4a (inset) shows an iso-energy contour at -5 meV, and the three-fold rotational symmetry is from the trigonal warping effect. Owing to the trigonal warping, the Dirac points arrange themselves along the three directions and at the centre²⁹. The black and white dots represent Dirac points with Berry phase π and $-\pi$, which are also labelled by the black and white arrows in the band structure. They appear at different energies and correspondingly different densities.

We also calculated the intrinsic contribution to the anomalous Hall conductivity by integrating the Berry curvature of the occupied states $\sigma^{\text{AHE}} = \int_{\text{occupied states}} \Omega$. Extended Data Fig. 4b shows the calculated Hall conductivity with respect to the doping density n_e and interlayer potential E_0 for a single valley and spin flavour. The hot spots at around -1.2×10^{12} cm⁻² and 0.4×10^{12} cm⁻² correspond to the four Dirac points at smaller k and the three Dirac points at larger k , respectively. In our valley-polarized half-metal picture, one valley has holes, whereas the other valley has zero net carriers ($n_e = 0$). As a result, to fully characterize the system, we need to add the contributions from the two valleys. Extended Data Fig. 4c shows the same plot as Extended Data Fig. 4b with the contribution from the other valley at zero density (opposite value to the dashed line in Extended Data Fig. 4b). Extended Data Fig. 4d provides a microscopic picture of the linear anomalous Hall conductivity with E . At $E = 0$, Berry curvature is zero everywhere except at the Dirac points, so σ^{xy} is zero. As E increases, Berry curvature hot spots emerge near the Dirac points and spread out. Consequently, there is more Berry curvature on states below E_F and σ^{xy} increases with E . Extended Data Fig. 4e shows line-cuts in Extended Data Fig. 4c from $n_e = 0$ to -0.5×10^{12} cm⁻² for a single spin copy. At a small interlayer potential E_0 , the Hall conductivity is roughly linear with E_0 . Extended Data Fig. 4f shows the measured σ^{xy} . The linear E dependence of σ^{xy} agrees with the calculated value qualitatively. We note that the measurements on the positive E side are affected by the contact issue at low temperatures (as can be seen from the n - E colour plot). The measured σ^{xy} is much larger than the calculated Berry curvature contribution, which could arise from extrinsic contribution⁴⁴. This phenomenon is also seen in other graphene-based orbital magnets—for example, the quarter-metal of rhombohedral trilayer graphene¹⁵.

Doping dependence of the orbital magnetism

We show the electric field dependence of the anomalous Hall effect (orbital magnetism) in the main text and here we present the doping dependence. Extended Data Fig. 5a is the same as Fig. 2c, and now we cut along the x -axis. Extended Data Fig. 5b,c shows magnetic hysteresis measured at $E = 5$ mV nm⁻¹ and $n_e = -2.5 \times 10^{11}$ cm⁻² to -9.5×10^{11} cm⁻² (corresponds to the dots with the same colour in Extended Data Fig. 5a) with temperatures of 0.3 K and 2 K. Clear magnetic hysteresis and anomalous Hall effect are seen within the waterdrop region, and we get the largest signal at around $n_e = -5.5 \times 10^{11}$ cm⁻². We also note that the magnetic coercive field at 2 K almost vanishes, aligned with the disappearance of the butterfly at 2 K.

Control the valley order with $\mathbf{E} \cdot \mathbf{B}$ field

Here we demonstrate $\mathbf{E} \cdot \mathbf{B}$ as the conjugate field of the valley order. Extended Data Fig. 6a,b shows the valley polarization corresponding to the R_{xy} plot in Fig. 3d,e with $B > 0$ and $B < 0$. The two hysteresis loops wind in opposite ways. However, if we plot the x -axis as the $\mathbf{E} \cdot \mathbf{B}$ field, the two loops will collapse into one, which demonstrates that the conjugate field of the valley is $\mathbf{E} \cdot \mathbf{B}$. Blue lines label scanning to positive E direction and yellow lines label scanning to negative E direction. The arrows indicate the scanning direction.

Random fluctuation of magnetization at $B = 0$

Extended Data Fig. 8 shows the fluctuation of R_{xy} as a function of time at $B = 0$ T. R_{xy} flips sign frequently with time, indicating the fluctuation of the magnetization because of the finite size of the magnet. The stochastic switching enables the system to act as a probabilistic bit, which is essential in probabilistic and neuromorphic computing^{45,46}. A small external B field (20 mT) is enough to stabilize the system to a controlled state without changing the ground state. As a result, our device is capable of shifting between the two operation modes (stochastic and controlled) easily.

R_{xy} measurement under different conditions

There are several measurement conditions, including scanning doping density or electric field and applying a small positive or negative B field. In Fig. 3a,b, we show the plots of scanning E with a positive magnetic field. In Extended Data Fig. 9, we discuss the results of other measurements (the applied magnetic field is ± 20 mT), and all four measurements are consistent with our picture.

1. Scan E , negative B (Extended Data Fig. 9a,b). Similar to Fig. 3a,b, the negative magnetic field now selects the opposite valley compared with the former case. The behaviour is the same as in Fig. 3a,b with an opposite sign of R_{xy} .
2. Scan n_e , positive B (Extended Data Fig. 9c,d). By contrast to the scanning E case, there is no butterfly-type hysteresis when scanning n_e , because the orbital magnetism of a valley does not change with n_e . The system will choose to polarize to the valley with magnetization parallel to B , resulting in positive R_{xy} in both positive and negative E sides. The magnetization of the system is small around $E = 0$, and the small external B field cannot effectively select a favoured valley, resulting in fluctuations around $E = 0$. We note that the fluctuations around $E = 0$ do not occur when scanning D because the system already chooses the valley as the system enters the VPHM state and stays in the chosen valley.
3. Scan n_e , negative B (Extended Data Fig. 9e,f). Similar to Extended Data Fig. 9c,d but with the opposite external B field. The small negative magnetic field will select the opposite valley compared with that of Extended Data Fig. 9c,d.

Hysteresis of the longitudinal resistance R_{xx}

In the main figures, we mainly show the R_{xy} behaviours and relate the jump of R_{xy} to the switching of the valley. In the extended data figures, we also present the R_{xx} behaviours corresponding to R_{xy} and show the R_{xx} jump simultaneously with R_{xy} .

Extended Data Fig. 10a–f shows the n - E map with a small positive magnetic field. Extended Data Fig. 10a,b is the same as Fig. 3a,b. Extended Data Fig. 10c,d is the R_{xx} map corresponding to Extended Data Fig. 10a,b. The white arrows indicate the jumps at the boundary, which matches where R_{xy} jumps. Extended Data Fig. 10e,f shows line-cuts at $n_e = -0.67 \times 10^{12} \text{ cm}^{-2}$, indicated by the dashed line in Extended Data Fig. 10c,d. The arrows label the scanning directions. The jumps in R_{xx} happen right before the system gets out of the VPHM state where R_{xy} also jumps. Extended Data Fig. 10g–l shows the data corresponding to the measurement in Fig. 4a,b, similar to Extended Data Fig. 10a–f. The R_{xx} jumps at the same time as the R_{xy} jumps. The hysteretic behaviours in R_{xx} indicate that the valley switching is a first-order process.

Extracting the average magnetic moment through a toy model

In Fig. 4g, we phenomenologically extracted the average magnetic moment per hole from the magnetic-field dependence and temperature dependence measurement of the R_{xy} - E butterfly. Our picture is depicted in Fig. 4f in which we assume that the barrier Δ does not change with magnetic field and temperature. The sweeping of the magnetic field in Fig. 4a,b was done very slowly (each scan takes about minutes). Therefore, in our toy model the system will switch to the valley with

lower energy (global minimum) when the magnetic energy added with thermal energy is larger than the barrier—that is, $\mathbf{M} \cdot \mathbf{B} + k_B T > \Delta$. Then we can estimate the average magnetic moment M at different E with the extracted critical electric field E_c at different magnetic fields and temperatures in Fig. 4e. We have

$$\begin{aligned} M(E_B)B(E_B) + k_B T(0.3K) &= \Delta \\ M(E_T)B(0.02T) + k_B T(E_T) &= \Delta \end{aligned}$$

where E_B and E_T are the critical electric fields when changing magnetic field and temperature. So the average magnetic moment can be written as

$$M(E_c) = (k_B T(E_T) - k_B T(0.3K)) / (B(E_B) - B(0.02T))$$

We extrapolate the data in Fig. 4e and calculate the average magnetic moment M as a function of the electric field and get Fig. 4g. We note that the absence of data at 1.5–2 K in Fig. 4e is because of the difficulty of stabilizing the sample temperature in this range in our experimental set-ups. When extracting the g -factor, we used the value of E_T by linear interpolation in this range.

Relation between ferro-valleytricity, ferroelectricity and magneto-electric effect

The coupling term $F = -\alpha EVB = -(\alpha EV)B = -E(\alpha VB)$ can be viewed as an orbital magnetic moment coupling to a magnetic field, as well as an electric polarization coupling to an electric field. In the main text, we discussed the orbital magnetism and here we elaborate on the electric polarization.

We note that the total electric polarization or dipole has two parts. Without considering the valley symmetry breaking, an electric dipole is induced by the gate electric field E . At gate electric field $E = 0 \text{ mV nm}^{-1}$, in both K and K' valleys, the conduction and valence band wave functions have 50% at the top layer and 50% at the bottom layer, preserving the inversion symmetry of the lattice structure. When a non-zero E is applied, the inversion symmetry is broken so that in both valleys the valence band wave function is polarized in the layer with a lower potential energy, whereas the conduction band wave function is polarized in the opposite layer. From the band structure point of view, applying a gate electric field opens up the band gap proportional to E and lowers the energy of the valence band (Extended Data Fig. 11a). The total energy lowering of the valence band and occupied states is equivalent to an electrostatic energy of $\mathbf{E} \cdot \mathbf{P}_0$, in which the electric dipole P_0 is induced by the applied E and characterizes the number of electrons the energy of which is affected by the gap opening. Although the electric potential energy includes a term that is $-\mathbf{E} \cdot \mathbf{P}_0$, we note that this energy should not be counted in the flipping process from K' to K: as explained above, P_0 is unrelated to valley polarization, so all the states on the free-energy curve in Fig. 4f have the same potential energy $-\mathbf{E} \cdot \mathbf{P}_0$ as they correspond to the same E and P_0 unrelated to valley polarization. As P_0 is unrelated to valley polarization, the ferro-valley order does not imply a ferroelectric order, because the system can have a big Fermi surface in the K valley and a small Fermi surface in the K' valley, even if the inversion symmetry is preserved, as shown by the states at the centre of the butterfly in Fig. 3c.

When the valley symmetry is spontaneously broken in the presence of a magnetic field B , the bands in K and K' valleys shift in energy because of the coupling between the orbital magnetization and B . This coupling results in the free energy $F = -\alpha EVB = -(\alpha EV)B$, where αEV is the average orbital magnetic moment as stated earlier. This same energy can be given as $F = -E(\alpha VB)$, where (αVB) is an effective electric dipole P' . This additional electric dipole P' is determined by both V and B , and it is involved in the ferro-valleytricity behaviour. From the band structure point of view, this electric dipole and the corresponding electrostatic energy can be seen from the shift of the

occupied states in the valence band in a magnetic field B (Extended Data Fig. 11b).

In the presence of B , P' (at $E = 0$ mV nm⁻¹) and valley polarization V should co-exist, as shown in Extended Data Fig. 11c. At a non-zero B , electron states form discrete Landau levels. Taking the zeroth Landau level as an example (other Landau levels have qualitatively similar sublattice and layer polarization, but quantitatively not as big as that in the zeroth Landau level), its electron wavefunctions in the K and K' valleys are located at the A and B sublattices, respectively. In all rhombohedral graphene, A and B sublattices to describe the lowest-energy bands are located at the top and bottom layers. Therefore, valley polarization leads to the imbalance of population of the zeroth Landau level, which results in a layer polarization of electric charge distribution and electric dipole.

In summary, ferro-valley order is not related to ferroelectricity when $B = 0$. Only with the presence of a magnetic field, the ferro-valley order leads to ferroelectricity such that $P' = (\alpha VB)$. To probe this ferroelectric order, a graphene-sensing layer or layer-sensitive capacitance measurement is required^{47–49}. We also note that when considering the free energy, we cannot consider the orbital magnetism and electric polarization at the same time, as they come from essentially the same term $F = -\alpha EVB$, and we should not double-count this energy.

The induced electrical polarization P' and orbital magnetic moment M can be viewed as a magneto-electric effect, in which the free energy $F = -\alpha VBE = -EP' = -BM$. The valley polarization V can be viewed as the coefficient of the magneto-electric effect, which can usually be controlled through strain in conventional multiferroic or magneto-electrics, for example.

Density and in-plane magnetic-field scan in the correlated insulating state at $D = n = 0$

We performed similar measurements as in ref. 18. Although the back-and-forth scans do not overlap perfectly (Extended Data Fig. 12), we did not see obvious hysteresis as reported in ref. 18.

Data availability

The data shown in the main figures are available at Harvard Dataverse (<https://doi.org/10.7910/DVN/Z2HKPY>). Other data that support the findings of this study are available from the corresponding author upon reasonable request.

41. Li, H. et al. Electrode-free anodic oxidation nanolithography of low-dimensional materials. *Nano Lett.* **18**, 8011–8015 (2018).
42. Han, T. et al. Correlated insulator and Chern insulators in pentalayer rhombohedral stacked graphene. Preprint at <https://arxiv.org/abs/2305.03151> (2023).
43. Zhang, F., Sahu, B., Min, H. & MacDonald, A. H. Band structure of ABC-stacked graphene trilayers. *Phys. Rev. B* **82**, 035409 (2010).
44. Tian, Y., Ye, L. & Jin, X. Proper scaling of the anomalous Hall effect. *Phys. Rev. Lett.* **103**, 087206 (2009).
45. Borders, W. A. et al. Integer factorization using stochastic magnetic tunnel junctions. *Nature* **573**, 390–393 (2019).
46. Mizrahi, A. et al. Neural-like computing with populations of superparamagnetic basis functions. *Nat. Commun.* **9**, 1533 (2018).
47. Fei, Z. et al. Ferroelectric switching of a two-dimensional metal. *Nature* **560**, 336–339 (2018).
48. de la Barrera, S. C. et al. Direct measurement of ferroelectric polarization in a tunable semimetal. *Nat. Commun.* **12**, 5298 (2021).
49. Hunt, B. M. et al. Direct measurement of discrete valley and orbital quantum numbers in bilayer graphene. *Nat. Commun.* **8**, 948 (2017).

Acknowledgements We acknowledge discussions with F. Zhang, J. Checkelsky, L. Levitov, Z. Dong, W. He, P. Yu, Y. Ba, F. Wang and L. Zhao. We acknowledge Y. Yao for his help in sample fabrication. L.J. acknowledges support from a Sloan Fellowship. Work by Tonghang Han was supported by the National Science Foundation (NSF) (grant no. DMR-2225925). The device fabrication of this work was supported by the STC Center for Integrated Quantum Materials (NSF grant no. DMR-1231319) and was carried out at the Harvard Center for Nanoscale Systems and MIT.nano. Part of the device fabrication was supported by USD (R&E) under contract no. FA8702-15-D-0001. K.W. and T.T. acknowledge support from the JSPS KAKENHI (grant nos 20H00354, 21H05233 and 23H02052) and the World Premier International Research Center Initiative, MEXT, Japan. L.F. was supported by the STC Center for Integrated Quantum Materials under NSF award no. DMR-1231319. H.P. acknowledges support from NSF (grant no. PHY-1506284) and AFOSR (grant no. FA9550-21-1-0216). A portion of this work was performed at the National High Magnetic Field Laboratory, which is supported by the NSF Cooperative Agreement no. DMR-2128556* and the State of Florida.

Author contributions Tonghang Han, Z.L., G.S., J.S. and J.W. performed the d.c. magneto-transport measurement. Tonghang Han and Tinayi Han fabricated the devices. K.W. and T.T. grew hBN single crystals. Tonghang Han performed the tight-binding calculations. H.P. and L.F. contributed to the data analysis. L.J. supervised the project. All authors discussed the results and wrote the paper.

Competing interests The authors declare no competing interests.

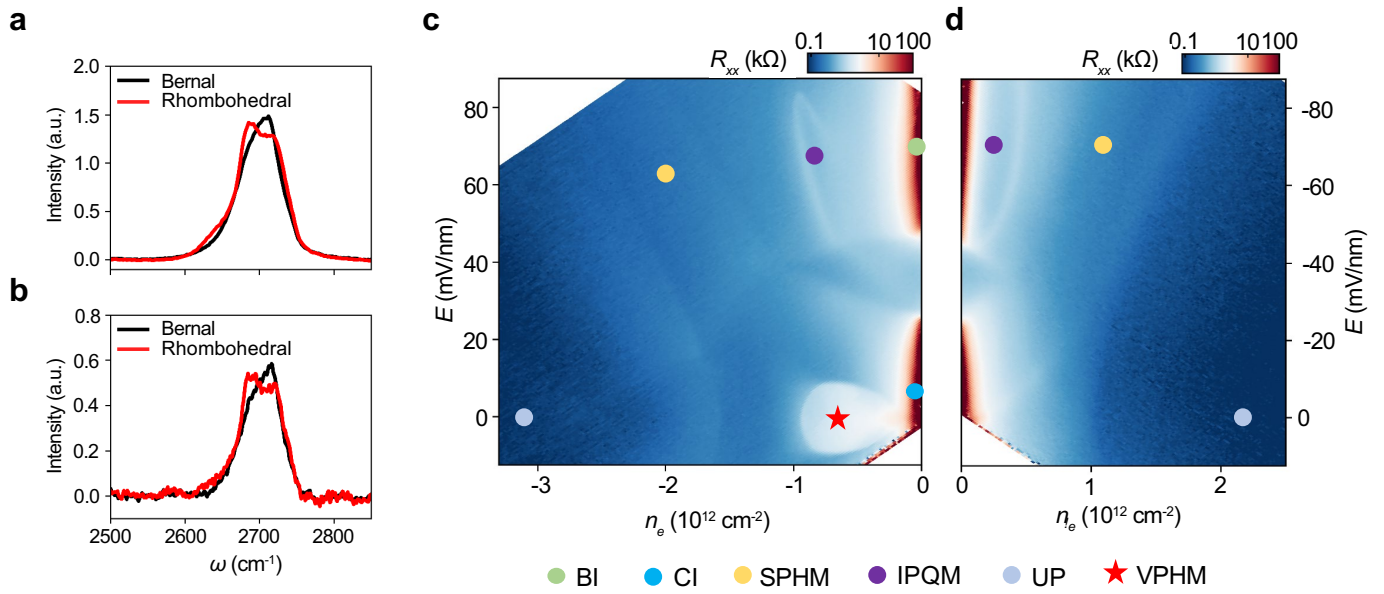
Additional information

Supplementary information The online version contains supplementary material available at <https://doi.org/10.1038/s41586-023-06572-w>.

Correspondence and requests for materials should be addressed to Long Ju.

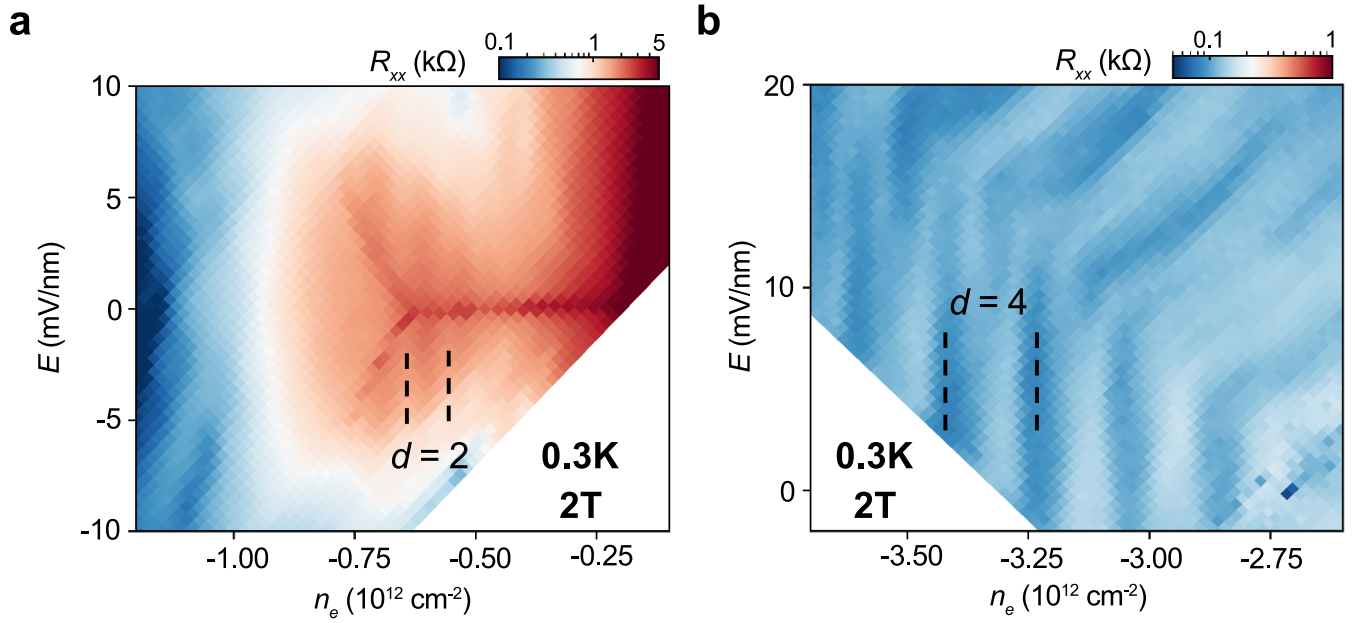
Peer review information *Nature* thanks Jianpeng Liu, Jianming Lu and the other, anonymous, reviewer(s) for their contribution to the peer review of this work. Peer reviewer reports are available.

Reprints and permissions information is available at <http://www.nature.com/reprints>.



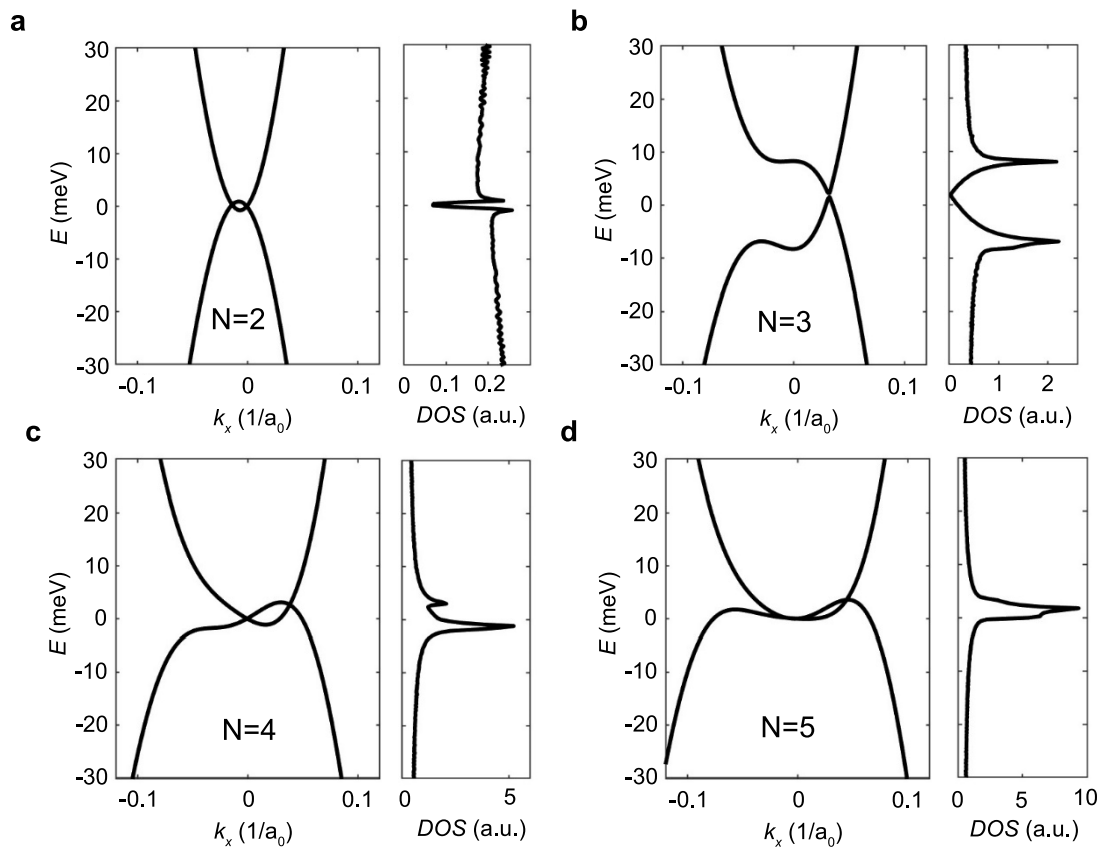
Extended Data Fig. 1 | Raman characterization and phase diagram of rhombohedral penta layer graphene. **a, b**, 2D Raman peak of Bernal (black) and rhombohedral (red) stacked pentalayer graphene before **(a)** and after **(b)** hBN encapsulation. The rhombohedral stacking is preserved after hBN encapsulation. **c, d**, Color plots of four-probe resistance R_{xx} as a function of carrier density n and displacement field E for the hole doping side **(c)** and

electron doping side **(d)** measured at $B = 0$ and a temperature of 100 mK. Colored dots label different phases including band insulator (BI), correlated insulator (CI), spin-polarized half metal (SPHM), isospin-polarized quarter metal (IPQM) and unpolarized metal (UP). The red star labels the valley polarized half metal (VPHM), which is the focus of the maintext. The details of IPQM and SPHM states can be found in ref. 42.



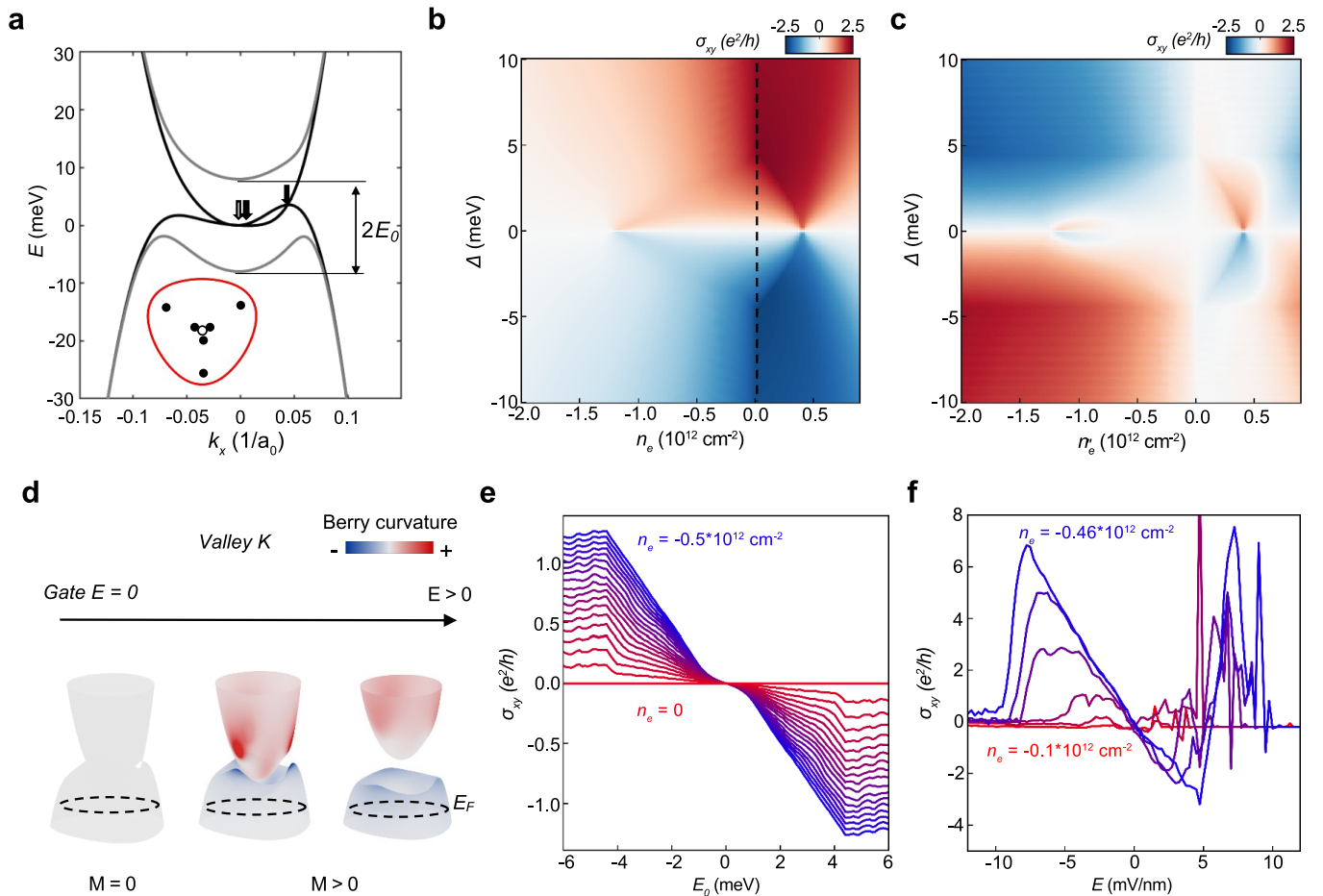
Extended Data Fig. 2 | Isospin degeneracy inferred from Landau level spacing. Color plots of four-probe resistance R_{xx} as a function of carrier density n and displacement field E for the small hole doping VPHM region (a) and large hole doping UP region (b) measured at $B = 2$ T and a temperature of

300 mK. The straight features correspond to Landau levels and the spacing indicates the degeneracy d of the band. With $d = 4$, all four isospin flavors are present at the Fermi surfaces. With $d = 2$, two out of four isospin flavors have Fermi surfaces (the so-called half-metal).



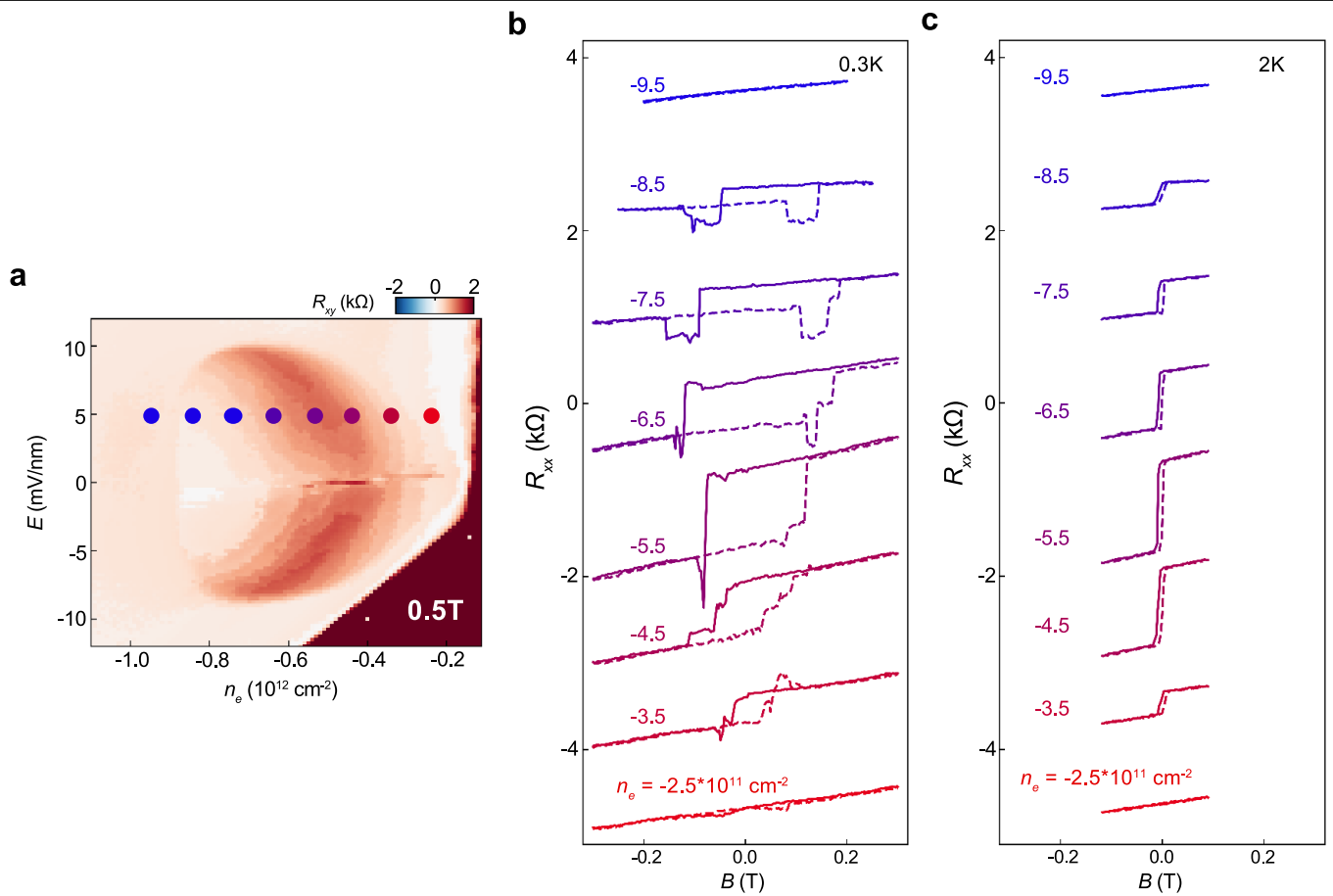
Extended Data Fig. 3 | Single particle band structure and density of states of rhombohedral stacked multilayer graphene. a–d, Tight-binding calculation of single particle band structure and density of states (DOS) for rhombohedral stacked multilayer graphene (layer number $N=2$ (a), 3 (b), 4 (c), 5 (d)). Due to the

remote hopping, the band structure deviates from $E \approx k^N$ at low energy. The rhombohedral pentalayer graphene has the flattest band among all layer numbers.



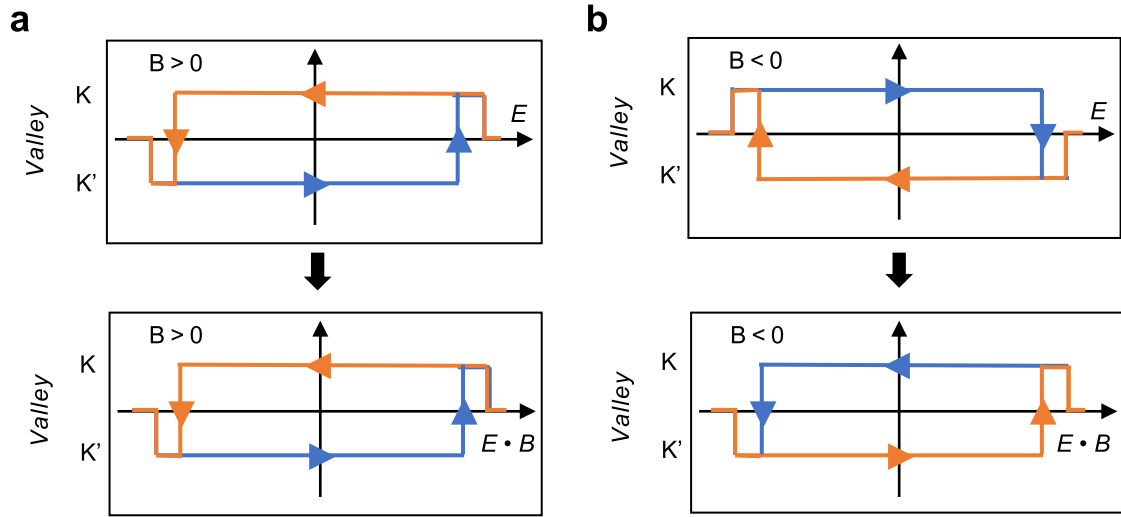
Extended Data Fig. 4 | Hall conductivity calculation. **a**, Tight-binding calculation of band structure for rhombohedral pentalayer graphene near the K point with an interlayer potential $2E_0 = 0$ meV (black) and 16 meV (grey). Inset shows an iso-energy contour at -5 meV and the black and white circles represent Dirac points with Berry phase π and $-\pi$, which are also labeled by the black and white arrows in the band structure. **b**, Calculation of Hall conductivity σ^{xy} with respect to the doping density n_e and interlayer potential E_0 for a single valley. The hot spots at around -1.2 and $0.4 \times 10^{12} \text{ cm}^{-2}$ correspond to the four Dirac points at smaller k and the three Dirac points at larger k respectively. **c**, The same plot as **b** with the contribution from the other valley at zero density (same position and opposite value to the dashed line in **b**). **d**, Colored-coded band structure in the K valley, showing the Berry curvature distribution at

varied gate electric field E_s . The iso-energy contour at Fermi level E_F is labeled by the dashed circle. σ^{xy} can be calculated by integrating the Berry curvature below E_F . At $E = 0$ mV/nm, Berry curvature is zero everywhere except for at the Dirac points, and σ^{xy} is zero. As E increases, Berry curvature hot spots emerge near the Dirac points and spread out. Consequently, there is more Berry curvature on states below E_F and σ^{xy} increases with E . **e**, Linecuts in **c** from $n_e = 0$ to $-0.5 \times 10^{12} \text{ cm}^{-2}$ for a single spin copy. At a small interlayer potential E_0 , the Hall conductivity is roughly linear with E_0 . **f**, Measured σ^{xy} at 20mT and 0.3 K. The linear E dependence of σ^{xy} agrees with the calculation qualitatively. Measurements on the positive E side suffer from contact issue at low temperatures.



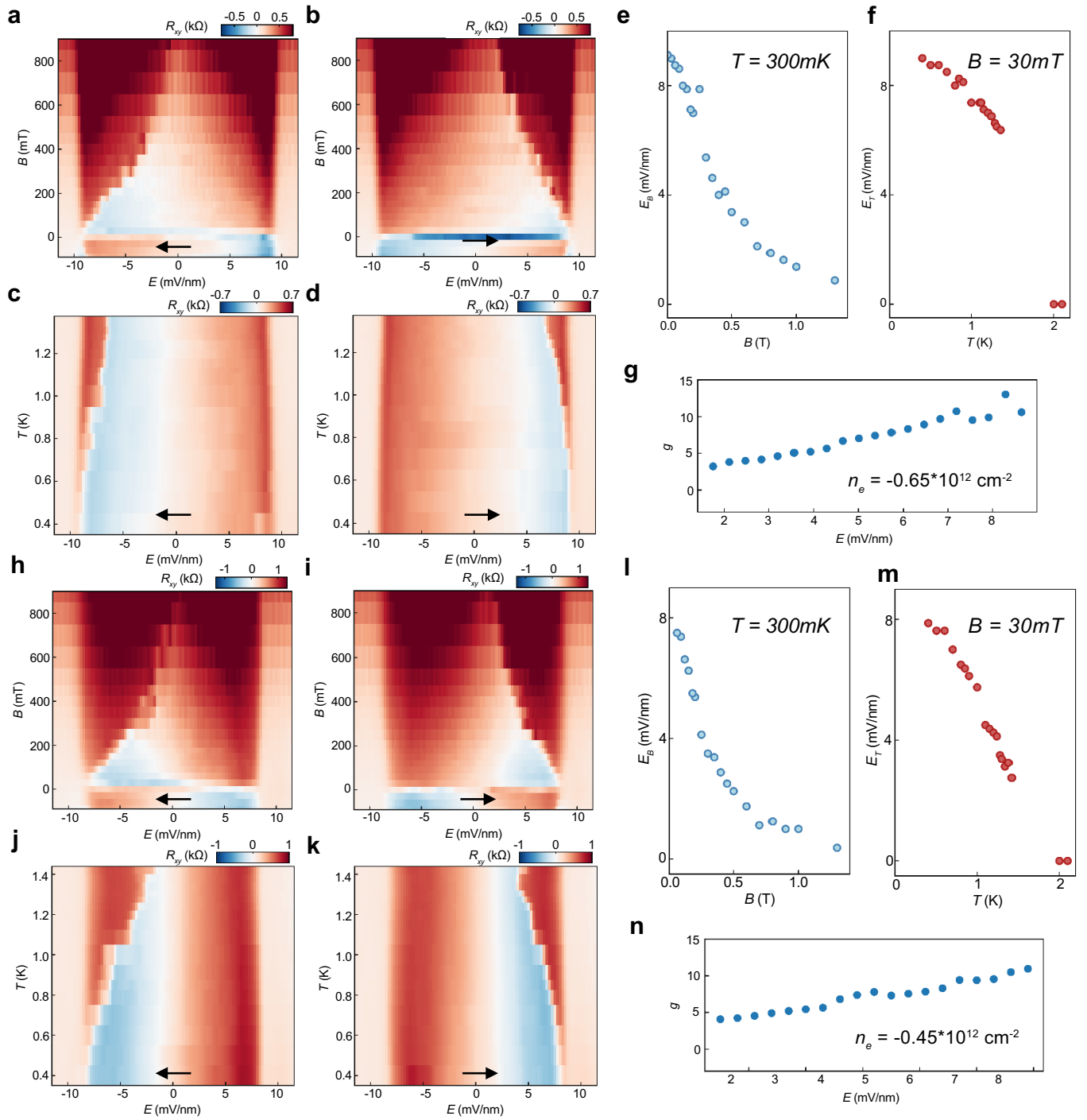
Extended Data Fig. 5 | Magnetic hysteresis at 0.3 K and 2 K at different doping. **a**, Color plots of four-probe resistance R_{xy} as a function of carrier density n and displacement field E for the small hole doping VPHM region at $B = 0.5$ T and $T = 0.3$ K. **b** & **c**, R_{xy} as the magnetic field B is scanned, showing clear hysteresis loops within the droplet region. Curves correspond to dots

with the same color in **a** at $E = 5$ mV/nm and different n_e at $T = 0.3$ K **a** and 2 K **b**, and are shifted vertically for clarity. Solid and dashed curves correspond to forward and backward scanning of the B field. At 2 K, the coercive field of magnetic hysteresis almost vanishes, consistent with the disappearance of the ferro-valleytronic order at 2 K.



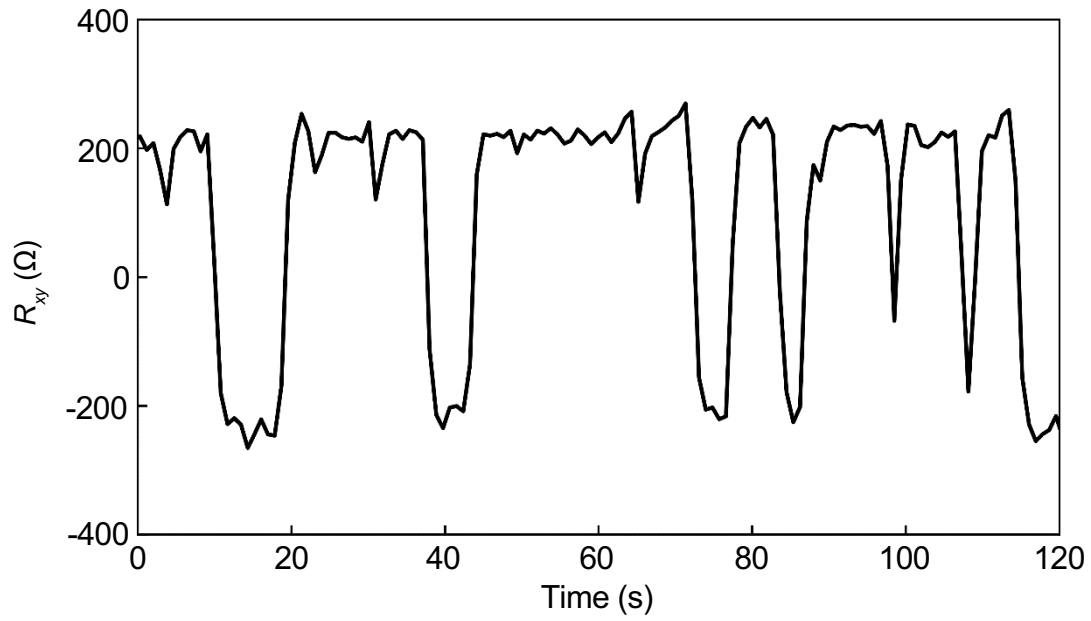
Extended Data Fig. 6 | Control valley with $E \cdot B$ field. a & b, Plots of valley polarization correspond to the R_{xy} plot in Figs. 3d and e with $B > 0$ (a) and $B < 0$ (b), featuring two hysteresis loops winding in opposite ways. However, if we plot the x-axis as the $E \cdot B$ field, the two loops will collapse into one, which

demonstrates that the conjugate field of the valley is $E \cdot B$. Blue (yellow) lines labels scanning to positive (negative) E direction. The arrows indicate the scanning direction.



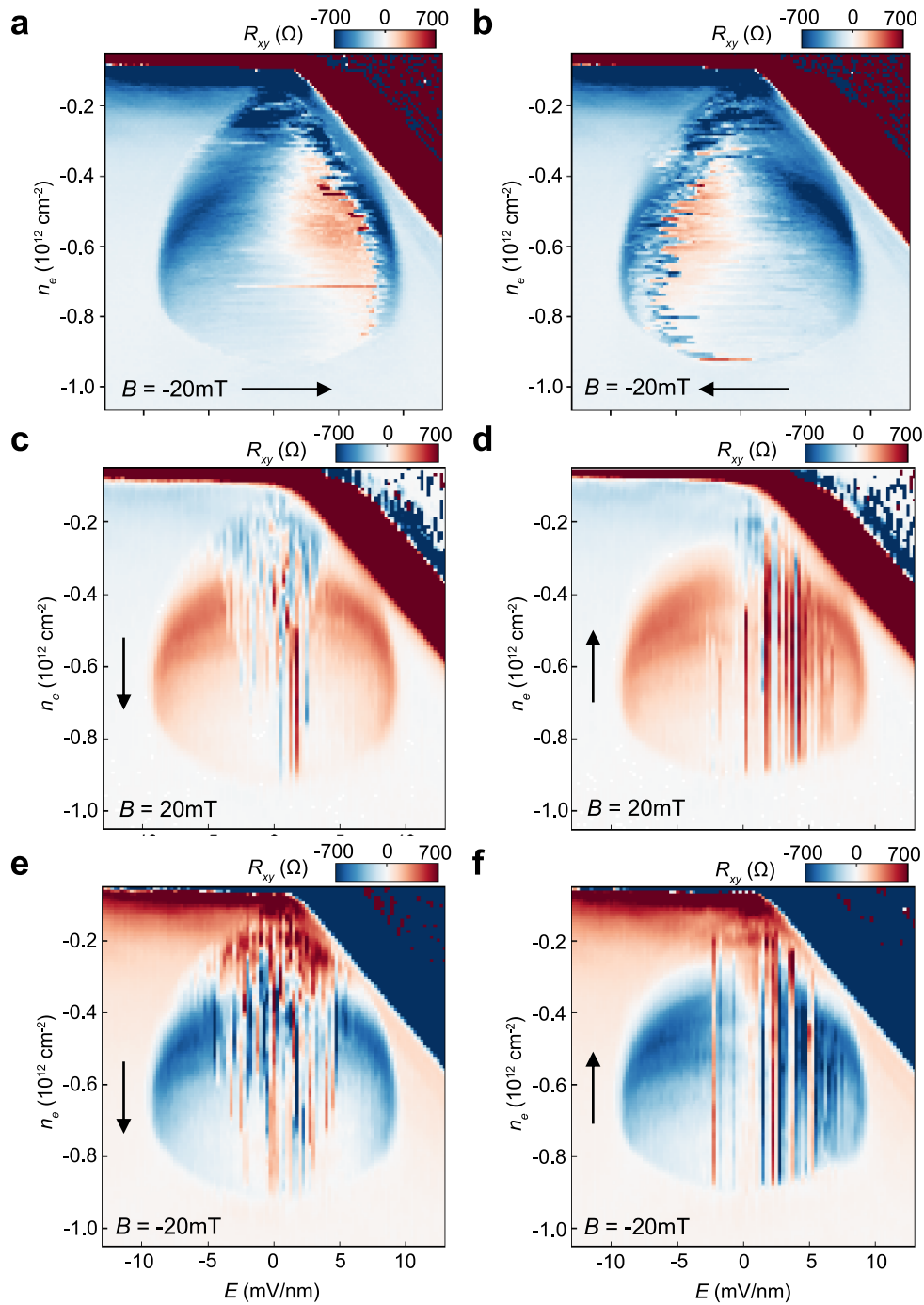
Extended Data Fig. 7 | Evolution of the 'butterfly' as a function of magnetic field and temperature at $n_e = -0.65 \times 10^{12} \text{ cm}^{-2}$ and $n_e = -0.45 \times 10^{12} \text{ cm}^{-2}$. a & b. R_{xy} as E is scanned at different magnetic fields at $n_e = -0.65 \times 10^{12} \text{ cm}^{-2}$. d & e. R_{xy} as E is scanned at different temperatures at $n_e = -0.65 \times 10^{12} \text{ cm}^{-2}$ and $B = 30 \text{ mT}$.

e & f. Critical fields E_B and E_T from a-d. g. Effective g -factor of the averaged orbital magnetic moment as a function of E extracted from e & f. h-n. Same measurements and analysis as a-g at $n_e = -0.45 \times 10^{12} \text{ cm}^{-2}$.



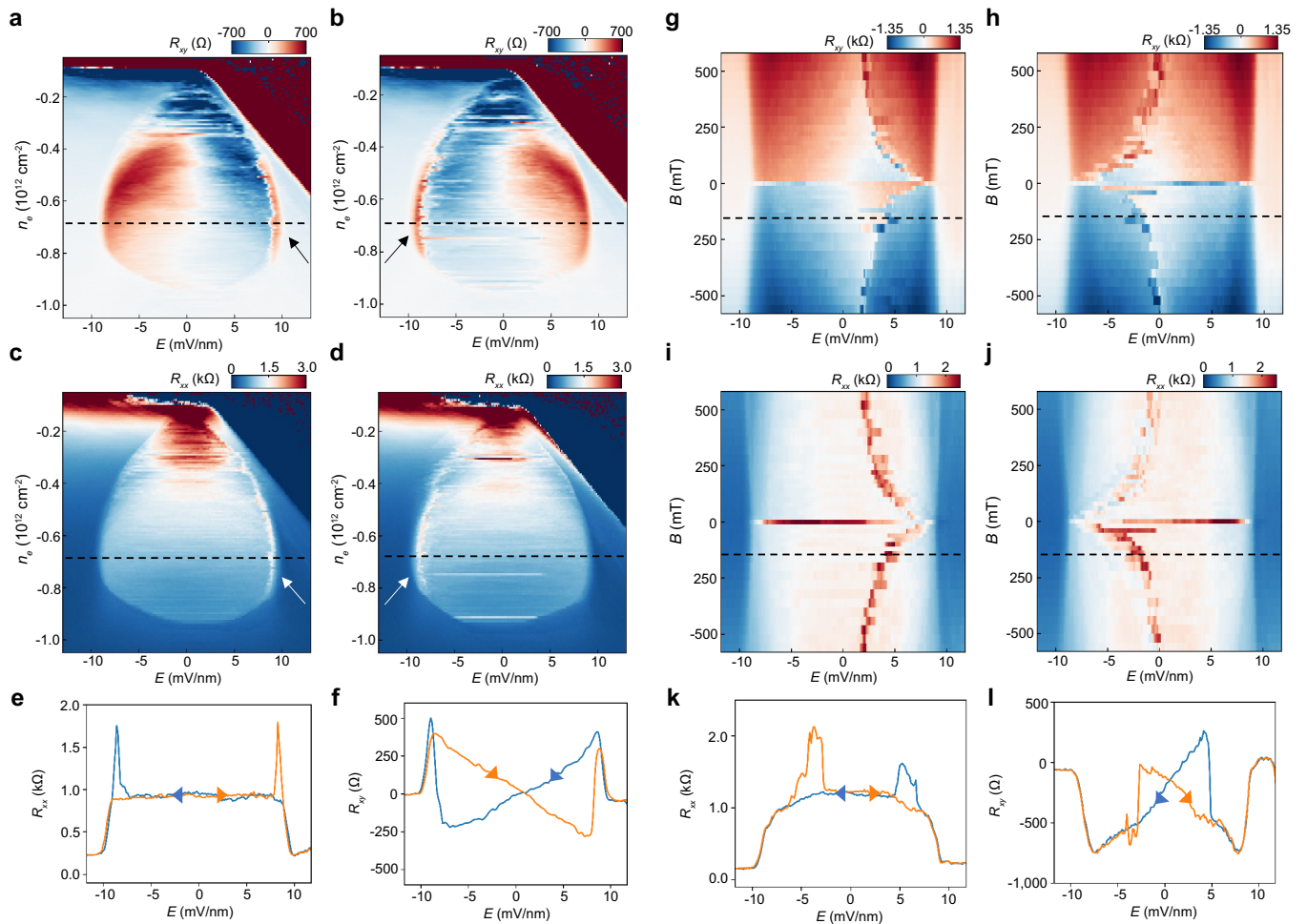
Extended Data Fig. 8 | Fluctuation of magnetization at zero magnetic field. R_{xy} as a function of time, measured at $n_e = -0.7 \cdot 10^{12} \text{cm}^{-2}$, $E = 4 \text{ mV/nm}$, $B = 0$ and $T = 300 \text{ mK}$. R_{xy} flips sign frequently with time, indicating the fluctuation of the

magnetization due to the finite size of the magnet. A small external B field (20mT) can stabilize the system without changing the ground state.



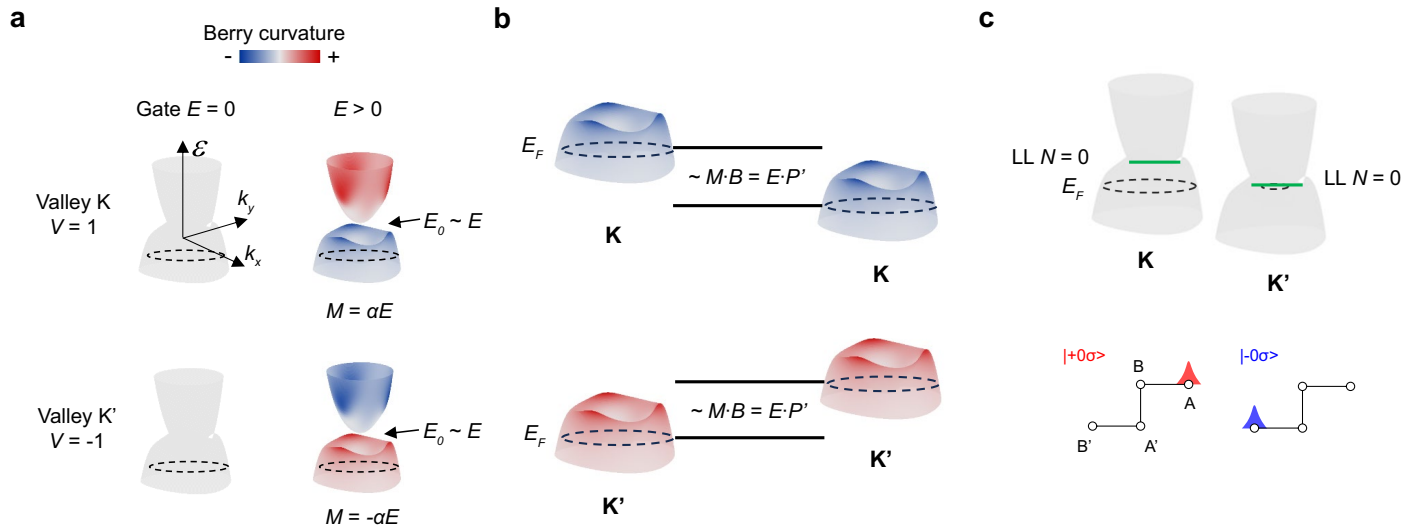
Extended Data Fig. 9 | Hall resistance behaviors under different measuring conditions. **a & b**, 2D color maps of R_{xy} in the droplet region corresponding to forward and backward scanning of E with a small negative magnetic field $B = -20 \text{ mT}$. **c & d**, The same plot as in **a** and **b** but with scanning density n_e at $B = 20 \text{ mT}$. **e & f**, The same plot as in **a** and **b** but with scanning density n_e with $B = -20 \text{ mT}$. R_{xy} changes the sign as we scan E but stays the same sign as we scan

n_e . This is due to the fact that the magnetic moment for a given valley will reverse as we scan E but not n_e . As we scan n_e , the system will choose to polarize to the valley with the magnetic moment parallel with external B . The random jumps near $E = 0$ when scanning n_e is because the magnetic moment near $E = 0$ is very small and the coupling to the external B field is weak, so the system cannot decide which valley to choose.



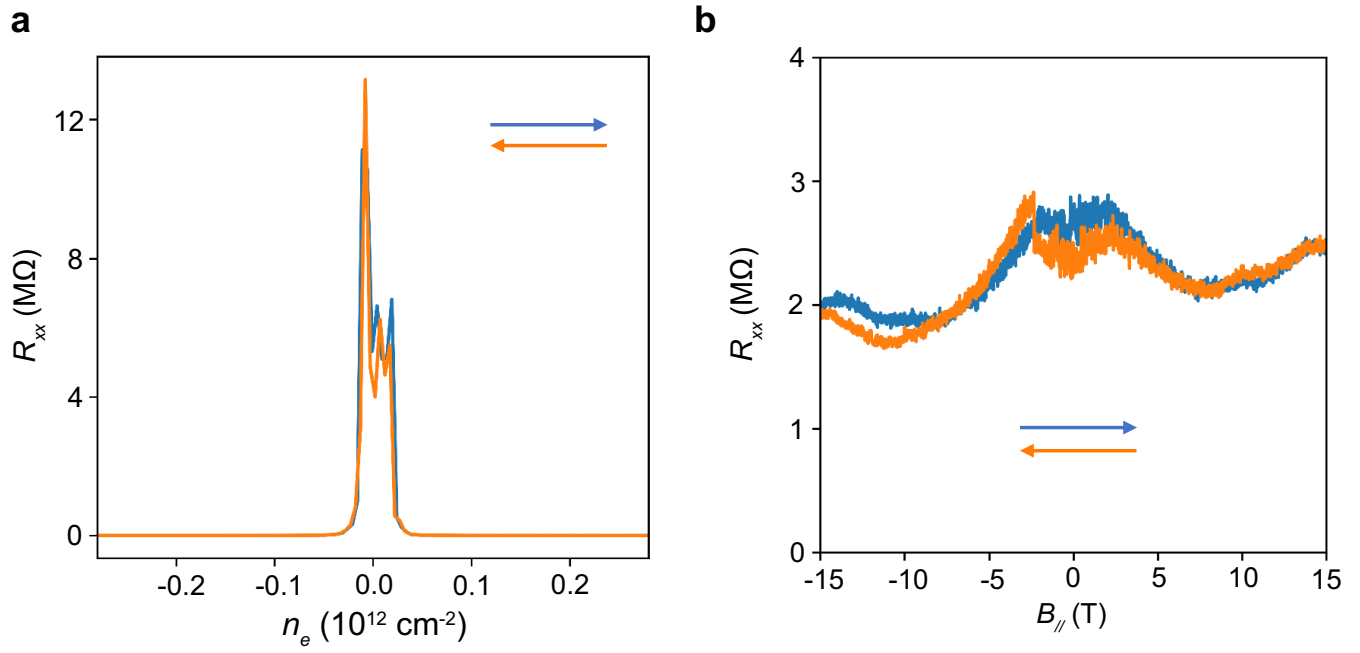
Extended Data Fig. 10 | Longitudinal resistance R_{xx} hysteresis. **a & b,** The same plot as Fig. 3d & e. The arrow indicates the jump in R_{xy} where the valley switches. **c & d,** The same plot as in **a & b** for R_{xx} . The arrow indicates where R_{xx} jumps and it also coincides with where the R_{xy} jumps. **e & f,** Linecuts of R_{xx} and R_{xy} at $n_e = -0.67 \times 10^{12}$ cm $^{-2}$ as indicated by the dashed line in **a-d**. **g & h,** The same

plot as Fig. 4a & b. **i & j,** The same plot as in **g & h** for R_{xx} . The jumps in R_{xx} correspond to that in R_{xy} . **k & l,** Linecuts of R_{xx} and R_{xy} at $B = -0.16$ T as indicated by the dashed line in **a-d**. The jumps in R_{xx} indicate the valley-switching is a first-order process.



Extended Data Fig. 11 | Ferro-valleytricity and ferroelectricity. a. The opening of the band gap E_0 by a gate electric field E is effectively inducing an electric dipole P_0 which couples to E and lowers the energy of the occupied states. The Berry curvature and orbital magnetization in the K and K' valleys are opposite. **b.** Given a non-zero E , the valence bands in the K and K' valley experience further shift in a magnetic field B . The shift is proportional to the orbital magnetization of the occupied states. This shift in energy $M \cdot B = \alpha E \cdot B$ can be viewed as $M \cdot B = E \cdot (\alpha B) = E \cdot P'$, where is effectively an additional electric

dipole P' . This latter part of electric dipole P' matters for the valleytricity while the P_0 does not. **c.** Ferro-electricity in the valley-polarized state at $E = 0, |B| > 0$. Upper panel: illustration of the valley polarization and imbalanced population of the zeroth Landau levels in K and K' valley at a non-zero B . Lower panel: valley and sublattice and layer have a one-to-one-to-one correspondence in the zeroth Landau level of rhombohedral graphene. Thus a valley polarization at non-zero B implies layer polarization and an electric dipole at $E = 0$ mV/nm. In this picture, ferro-electricity should exist at $E = 0$ mV/nm and $|B| > 0$ mT.



Extended Data Fig. 12 | Density and in-plane magnetic field scan at $E=0$. **a.** R_{xx} versus forward and backward scanning of n . **b.** R_{xx} versus forward and backward scanning of $B_{//}$.